Pharmacological Regulation of Neural Circuit Formation in hIPSC-Derived Neurons and 'Mini-Brains'

by

Taylor Lee Rudisill

July, 2018

Director of Thesis: Karen Litwa

Major Department: Anatomy and Cell Biology

Emerging evidence suggests that altered neural connectivity, particularly at the level of synaptic connections, contributes to the pathology of many neurodevelopmental and neurodegenerative diseases. For instance, post-mortem Autistic patient brain samples have increased numbers of excitatory to inhibitory synaptic connections, referred to as an E/I imbalance [42]. Contrastingly, post-mortem brain samples from patients diagnosed with Alzheimer's disease have decreased numbers of synaptic connections [42]. In order to understand the mechanisms that underlie the formation of these synaptic circuits, we develop 3-D human cortical organoids ('mini-brains') from human-induced pluripotent stem cells (hIPSCs).

Previous research demonstrates that rearrangements of the actomyosin cytoskeleton drive neural circuit formation, in particular the development and maturation of actin-enriched spines at excitatory synapses. This thesis work investigates how pharmacological regulation of actomyosin activity affects neuronal connectivity during neurite formation in 2-D and excitatory synapse formation in 3-D 'mini-brains'. The Rho-

Kinase (ROCK) inhibitor, Y-27632, both inhibits non-muscle myosin II (NM-II) and leads to a corresponding increase in Rac-driven actin polymerization. In 2-D, Y-27632 promotes neurite formation. Specifically, Y-27632 increases the number, length, and branching of neurites in hIPSC-derived neurons. Furthermore, Y-27632 increases neurite persistence, while decreasing neurite protrusion and retraction rates. However, in 3-D, acute Y-27632 treatment increases excitatory synapse area, consistent with an increase in Rac-driven actin polymerization [39].

Thus, Y-27632 increases both neurite outgrowth and excitatory synapse formation and may serve as a potential therapeutic for neurodegenerative diseases associated with synapse loss such as Alzheimer's disease. This study demonstrates the need for physiologically-relevant brain models, such as 3-D cortical organoids, to assess the impact of drug therapies on developing neural circuits to potentially treat neurodevelopmental and neurodegenerative disorders.

Pharmacological Regulation of Neural Circuit Formation in hIPSC-Derived Neurons and 'Mini-Brains'

A Thesis

Presented to the Faculty of the Department of Anatomy and Cell Biology

East Carolina University

In Partial Fulfillment of the Requirements for the Degree

Master of Science Biomedical Science

by

Taylor Lee Rudisill

July, 2018

Pharmacological Regulation of Neural Circuit Formation

in hIPSC-Derived Neurons and 'Mini-Brains'

by

Taylor Lee Rudisill

APPROVED BY:

DIRECTOR OF THESIS: _____

Karen Litwa, Ph.D.

COMMITTEE MEMBER: _____

Christopher Geyer, Ph.D.

COMMITTEE MEMBER: _____

Qun Lu, Ph.D.

COMMITTEE MEMBER: _____

Ann Sperry, Ph.D.

PROGRAM DIRECTOR: _____

Richard Franklin, Ph.D.

DEAN OF THE

GRADUATE SCHOOL: _____

Paul J. Gemperline, Ph.D

ACKNOWLEDGEMENTS

Foremost, I would like to thank Dr. Litwa for giving me the opportunity to join your lab. I couldn't have imagined a better Principal Investigator. Thank you for guiding me through my research project and having patience with me as your very first graduate student. I also would like to thank our wonderful laboratory technician Brenna Kirk. Thank you for the countless number of things you do for our lab. Additionally, thanks to all other members of the Litwa lab that have supported me throughout my laboratory experience. Finally, thanks to my thesis committee members who provided valuable insight into my project.

TABLE OF CONTENTS

LIST OF TABLES

LIST OF FIGURES

LIST OF SYMBOLS OR ABBREVIATIONS

ActB	-Beta Actin
ANOVA	-Analysis of Variance
ASD	-Autism Spectrum Disorder
BDNF	-Brain-derived Neurotrophic Factor
bFGF	-Basic Fibroblast Growth Factor
BMP	-Bone Morphogenetic Protein
cAMP	-Cyclic Adenosine Monophosphate
DMEM/F-12	-Dulbecco's Modified Eagle Medium/Nutrient Mixture F-12
DCX	-Doublecortin
ECM	-Extracellular Matrix
EGF	-Epidermal Growth Factor
Ena/VASP	-Enabled/Vasodilator-Stimulated Phosphoprotein
Eps 8	-Epidermal Growth Factor Receptor Kinase Substrate 8
FDA	-U.S. Food and Drug Administration
FRET	- Förster Resonance Energy Transfer
GAPs	-GTPase Activating Proteins
GDNF	-Glial Cell-derived Neurotrophic Factor
GEFs	-Guanine Nucleotide Exchange Factors
hIPSCs	-Human-Induced Pluripotent Stem Cells
LIMK	-LIMK-Kinase 1
LTP	-Long-Term Potentiation
mEGFP	-Monomeric Enhanced Green Fluorescent Protein

‘Mini-brains’	-3-D Human Cortical Organoids
MLCP	-Myosin Light Chain Phosphatase
MTA	-Material Transfer Agreement
NM-II	-Non-Muscle Myosin II
NPCs	-Neural Progenitor Cells
NT3	-Neurotrophic factor 3
PAK	-p21-activated Kinase
PBS	-Phosphate-buffered Saline
pCofilin	-Phosphorylated Cofilin
pLIMK	-Phosphorylated LIMK-Kinase 1
pORN	-Poly-L-Ornithine
pRLC	-Phosphorylated (S19/S20) Myosin Light Chain/Regulatory Light Chain
PSD	-Post-Synaptic Density
RIPA	-Radioimmunoprecipitation assay buffer
RLC	-Myosin Light Chain/Regulatory Light Chain
ROCK	-Rho-Kinase
TGF-ß	-Transforming Growth Factor Beta
Vglut-1	-Vesicular Glutamate Transporter 1
WASP	-Wiskott–Aldrich Syndrome Protein

LIST OF DIAGRAMS

CHAPTER 1: INTRODUCTION

Idiopathic Autism

Autism spectrum disorder (ASD) is a genetically complex heterogeneous neurodevelopmental disorder in which patients exhibit social deficits in both verbal and non-verbal forms of communication and display restricted and repetitive behaviors [2]. More than 3.5 million Americans live with ASD, costing the United States nearly $250 billion annually in ASD-related services [2]. Most alarmingly, ASD is also the fastest growing developmental disability in the United States [45]. The prevalence of ASD in the United States has increased from an estimated 1 in 150 births in 2000 to a staggering 1 in 68 births in 2010 and 1 in 59 births in 2014 [3, 4, 45]. Unfortunately, there is no cure for ASD although early diagnosis and prevention can improve symptoms [2]. Moreover, there is no known single cause of ASD, but it is generally accepted that ASD is caused by abnormalities in brain structure and/or function [2]. Most recent evidence suggests that altered neural connectivity, particularly at the level of synaptic connections, contributes to the pathology of ASD. Specifically, ASD patients have increased densities of dendritic spines and an increased ratio of excitatory to inhibitory synaptic connections, referred to as an E/I imbalance [42]. In this study we explore a potential ASD therapeutic, Y-27632, due to its possible role of decreasing these abnormalities by altering the formation and maturation of dendritic spines.

Altered Dendritic Spine Density and Morphology

Dendritic spines function as the primary sites of excitatory neurotransmission, underlying learning and memory formation [60]. These actin-enriched spines synapse with pre-synaptic axon terminals, mediating electrochemical communication between neurons to form circuits that support normal brain development and cognitive function [60]. However, altered synaptic plasticity, in particular the density and morphology of dendritic spines, contributes to neurodevelopmental and neurodegenerative diseases such as Autism and Alzheimer's Disease [42].

In early post-natal development, a robust increase in dendritic spines is refined in an activity-dependent manner to strengthen specific neuronal connections while eliminating others, ultimately resulting in a relatively steady-state level of synaptic connections that persists throughout adulthood [Diagram 1, black] [42]. In neurodevelopmental disorders, such as Autism, defects in eliminating synaptic connections may result in the elevated dendritic spine density observed in post-mortem patient brain samples and animal models [Diagram 1, pink] [42]. Conversely, in neurodegenerative disorders, such as Alzheimer's Disease, excessive spine loss promotes cognitive decline prior to neuronal cell death [Diagram 1, blue] [42].

Identification of the mechanisms that sculpt specific stages of synapse formation, maturation, pruning, and activity-dependent remodeling will allow for therapeutic intervention at discrete developmental and pathological stages. Thus, it is imperative to understand the regulatory mechanisms that remodel synaptic architecture during development and in response to excitatory/inhibitory activity.

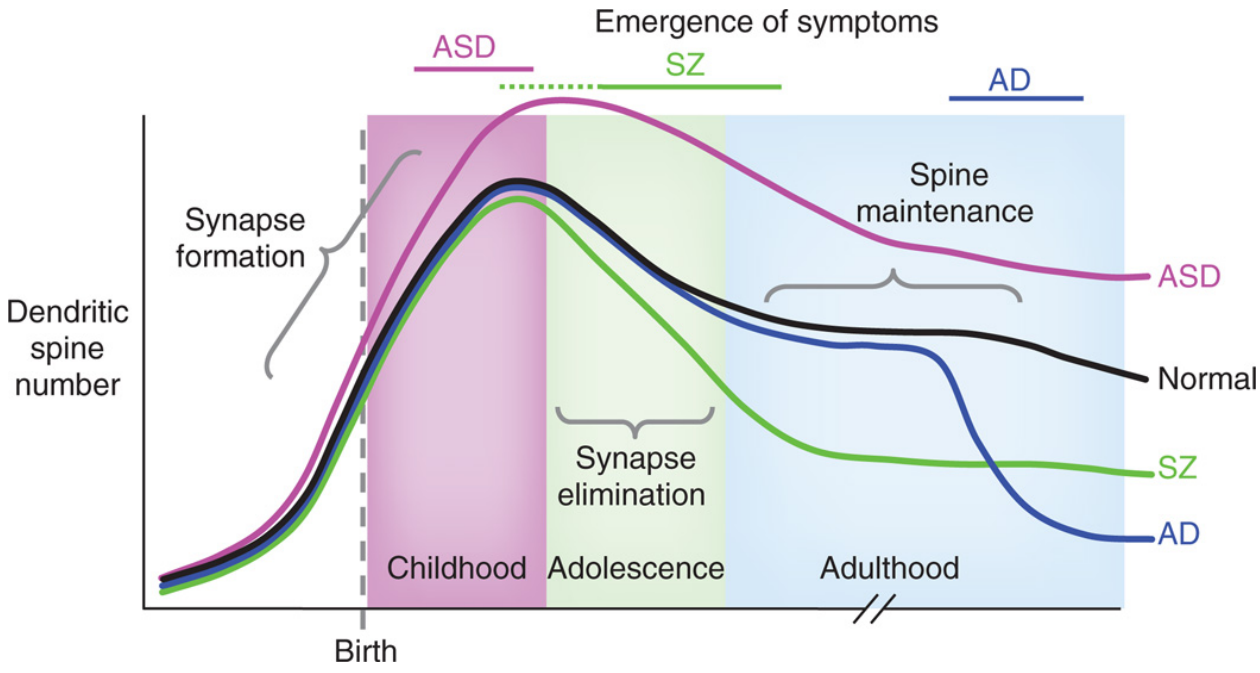

Diagram 1. Putative Lifetime Trajectory of Dendritic Spine Number. In normal subjects (black), spine numbers increase before and after birth; spines are selectively eliminated during childhood and adolescence to adult levels. In ASD (pink), exaggerated spine formation or incomplete pruning may occur in childhood leading to increased spine numbers. In schizophrenia (green), exaggerated spine pruning during late childhood or adolescence may lead to the emergence of symptoms during these periods. In Alzheimer's disease (blue), spines are rapidly lost in late adulthood, suggesting perturbed spine maintenance mechanisms that may underlie cognitive decline. Bars across the top indicate the period of emergence of symptoms and diagnosis. (Figure from Penzes et al. [42], legend modified)

Actin Dynamics Underlie Dendritic Spine Maturation and Synapse Formation

Dendritic spines consist primarily of actin and actin-associated proteins [Diagram 2] [17]. During spinogenesis, spines emerge from patches of branched actin along dendritic shafts [Diagram 2A] as filopodia-like spine precursors with anti-parallel actin filaments that associate with the actin motor protein, non-muscle myosin II (NM-II) [Diagram 2B] [17, 27]. Epidermal growth factor receptor kinase substrate 8 (Eps8) inhibits this process by capping the ends of barbed actin, preventing further actin polymerization and lengthening of spine precursors [Diagram 2A] [17, 34]. Conversely, enabled/vasodilator-stimulated phosphoprotein (Ena/VASP) family proteins may induce the formation of filopodia-like spine precursors due to their anti-capping properties [Diagram 2A] [8, 17].

These filopodia-like spine precursors subsequently [Diagram 2B] mature into thin spines with a distinct spine head and neck [Diagram 2C] [17, 59]. Further excitatory stimulation leads to spine maturation into a polarized mushroom-shape, consisting of a constricted neck and bulbous spine head with a post-synaptic density (PSD) that clusters neurotransmitter receptors across from the pre-synaptic axon terminal [Diagram 2D] [17]. Actin-associated proteins exhibit preferential localization to discrete regions within mature spines [27]. For example, Arp2/3 and capping protein, which regulate actin filament assembly, preferentially localize to the spine head, while myosin-II, which bundles and contracts actin filaments, preferentially localizes to the spine neck and lower portion of the spine head [27]. Despite these detailed insights into the molecular architecture of the

spine, the regulatory mechanisms that drive actin dynamics at specific stages of synaptic development are not well understood.

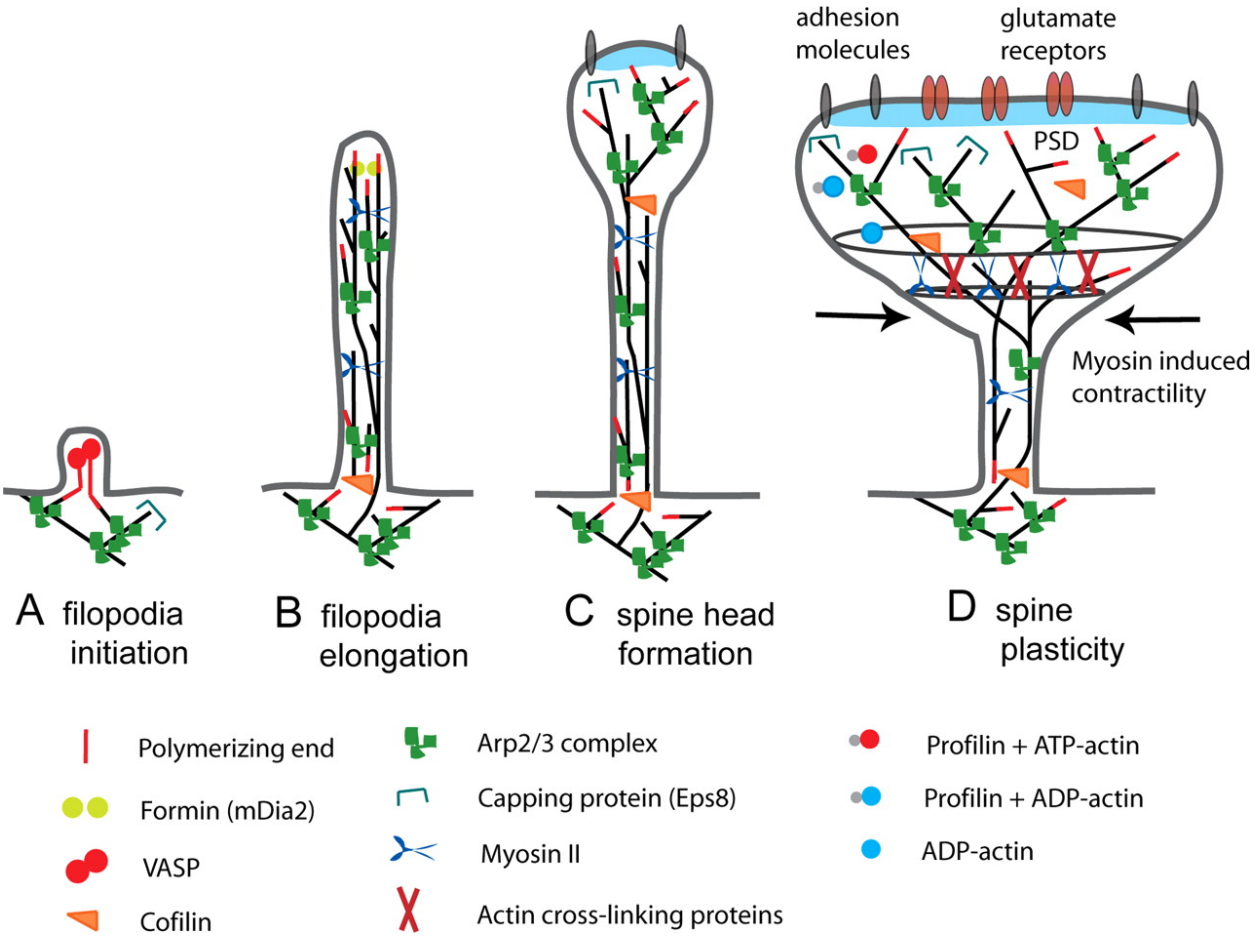

Diagram 2. Actin Regulatory Mechanisms During Spine Development and Plasticity. (A) Initiation of the dendritic filopodium and its elongation. Eps8 inhibits filopodia initiation by its capping activity. Ena/VASP proteins may induce filopodia elongation from Arp2/3 complex–generated branched filaments by anti-capping the actin barbed ends. (B) mDia2 promotes actin filament polymerization in the filopodium tip. The factors driving actin filament polymerization in the base of filopodia remain to be identified. (C) Extensive actin branching occurs at the filopodium tip and the spine head begins to form. The rate of actin assembly is now increased and the large Arp2/3-nucleated branched actin filament network leads to enlargement of the spine head. The function of ADF/cofilins, in addition to replenishing the cytoplasmic actin monomer pool in neurons, is to control the proper length of actin filaments and thus to prevent formation of abnormal protrusions from spine heads. (D) Mature spines are still dynamic but maintain their overall morphology. Myosin II–dependent contractility and cross-linking of actin filaments further modulate the shape of the spine head. (Figure from Hotulainen et al. [17], legend modified)

Master Regulators of the Actin Cytoskeleton

RhoGTPases regulate actin cytoskeleton organization and dynamics in diverse cellular processes, including dendritic spine morphogenesis [40, 54]. Coordinated activity of the small RhoGTPases, RhoA, Rac1, and Cdc42, orchestrate synaptic development and plasticity [15, 44]. Rac1 and Cdc42-driven actin polymerization regulates spine precursor formation and elongation through actin regulatory proteins, such as profilin and LIM-Kinase1 (LIMK) [18, 20, 33]. However, Rac1/Cdc42-driven actin polymerization also promotes spine head and post-synaptic density (PSD) expansion underlying synaptic strengthening [11, 15, 20, 52]. Conversely, RhoA antagonizes spine precursor formation, but is required for synaptic maturation via activation of the actin motor protein, NM-II, which polarizes the spine into the mature mushroom-shape morphology, although further NM-II activity may cause spine and dendrite retraction [Diagram 3] [16, 33, 39, 44].

Proper regulation of RhoGTPase signaling pathways is crucial for the consolidation and persistence of long-term potentiation (LTP) underlying learning and memory formation [38]. For example, loss of Rac1/Cdc42 effector kinases, PAK3 or LIMK1, alters spine morphology and LTP, resulting in non-syndromic mental retardation and Williams Syndrome, respectively [38, 53]. Thus, RhoGTPase-mediated spine morphological changes support normal neuronal function underlying cognitive abilities.

In addition to these downstream regulators, small RhoGTPases are themselves regulated due to their low intrinsic GTPase activity [14]. Guanine nucleotide exchange factors (GEFs) promote the exchange of GDP for GTP, activating RhoGTPases, while GTPase activating proteins (GAPs) promote GTP hydrolysis to GDP, resulting in

RhoGTPase inactivation [14]. Similar to downstream effectors, mutations in RhoGTPase regulators, such as the Rac1 GEF, β-PIX, or RhoA GAP, oligophrenin-1, result in neurodevelopmental disorders, such as non-syndromic mental retardation [38].

Recent studies have begun to delineate when specific RhoGTPase regulators function in synaptic development. For example, the Rac1 GEF β-PIX promotes dendritic spine initiation while the Cdc42 GEF Frabin and RhoA GAP oligophrenin-1 stimulate spine precursor elongation [33]. Furthermore, a novel Rac1 GAP, ArhGAP23, functions specifically to promote stabilization of the mature mushroom-shape spine [33]. These findings begin to address how specific RhoGTPases and their regulators function temporally within dendritic spines to shape brain development and how their misregulation may contribute to neurodevelopment disorders, such as Autism.

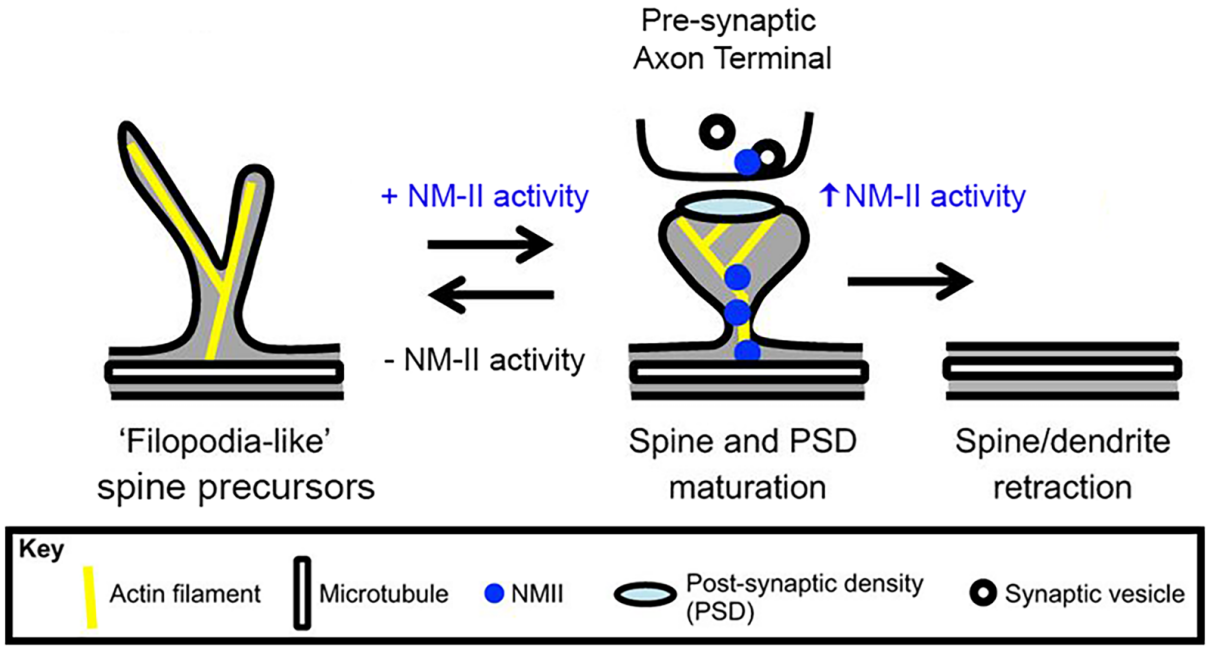

Diagram 3. NM-II Regulates Neuronal Plasticity. NM-II drives dynamic changes in neuronal morphology, including changes in dendritic spine formation and maturation. At the post-synaptic spine, NM-II drives changes in actin organization that regulate spine and PSD morphology and size, whereas, on the pre-synaptic side, NM-II participates in synaptic vesicle recycling. The absence or inhibition of NM-II activity results in dynamic 'filopodia-like' spine precursors and prevents spine maturation. In contrast, NM-II activity drives spine and PSD maturation, although further NM-II activity might result in spine and even dendrite retraction. (Figure adapted from Newell-Litwa et al. [40], legend modified)

Y-27632: A Potential ASD Therapeutic

Given our current understanding of RhoGTPase regulation of actin-driven dendritic spine maturation and synapse formation, it is hypothesized that downregulation of NM-II may decrease the density of mature mushroom-shaped spines and lower E/I imbalances in ASD patients. As mentioned previously, NM-II activity is necessary for dendritic spine maturation and synapse formation due to its polarization of the dendritic spine [Diagram 3] [16, 33, 39, 44]. Specifically, NM-II contracts actin filaments into actomyosin filament bundles, known as stress fibers [Diagram 4] [6, 14, 56]. These stress fibers, located mainly in the spine neck and lower portion of the spine head, contract actin filaments of filopodia-like spine precursors to create spines of the mature mushroom-shaped morphology, leading to synapse formation [16, 33, 39, 44]. Thus, if NM-II activity was downregulated, less mature mushroom-shaped spines may form, leading to the formation of less excitatory synapses. To test this hypothesis, the Rho-Kinase (ROCK) inhibitor Y-27632 was utilized to decrease NM-II activity [Diagram 4].

ROCK is a serine/threonine effector kinase of the RhoGTPase RhoA that activates NM-II by phosphorylation of its myosin regulatory light chain (RLC) [1] [Diagram 4]. There are two ROCK isoforms, ROCK1 and ROCK2, which phosphorylate and activate NM-II. Specifically, ROCK1 diphosphorylates threonine 18 and serine 19 residues of RLC, while ROCK2 monophosphorylates serine 19 of RLC [39]. This difference in phosphorylation underlies the distinctive functional roles of ROCK1 and ROCK2. In ROCK2 knockdown experiments, ROCK1 activity alone produces stable stress fibers that drive PSD maturation of dendritic spines and define the rear of a cell. [16, 39, 55]. However, in

ROCK1 knockdown experiments, ROCK2 activity alone leads to the formation of less stable stress fibers that produce filopodia-like dendritic spine precursors with smaller PSDs, but promote focal adhesion formation in migratory cell protrusions [16, 39, 55]. Both ROCK1 and ROCK2 further increase NM-II activity by inhibition of myosin light chain phosphatase (MLCP), a protein that inactivates NM-II by removal of phosphate groups from the RLC of NM-II [Diagram 4] [24]. Therefore, a ROCK inhibitor decreases NM-II activity by decreasing RLC phosphorylation and increasing MLCP-mediated RLC dephosphorylation.

The effects of ROCK inhibition on neurite formation have been well-studied. Particularly, ROCK inhibition has been shown to increase neurite outgrowth in cultured human NT2 cells [29, 46], human PC-12 cells [36, 57], and mouse neural stem cells [13, 21]. Together, these studies point to a ROCK inhibitor-mediated dose-dependent and time-dependent increase in neural generation and neurite length. Given these findings, ROCK inhibitors may serve as a potential therapeutic for nerve regeneration [28, 51]. Despite our current understanding of ROCK inhibition on neurite formation, less is known in the context of dendritic spines. Y-27632-mediated ROCK inhibition has been shown to create filopodia-like spines in rat hippocampal neurons [16], but further experiments are needed to determine how this altered dendritic spine morphology is affecting synaptic connections. Furthermore, we need a physiologically-relevant system to address the role of Y-27632 in both neurite formation and spine morphogenesis.

In this thesis work, we expand on the current knowledge of ROCK inhibition on early neurite formation in a human-induced pluripotent stem cell (hIPSC)-derived neuron

model in 2-D. In particular, we explore the effects of Y-27632-mediated ROCK inhibition on neurite formation, elongation, and branching. Additionally, we investigate the neurite dynamics of differentiating cells to better understand the mechanisms underlying these Y-27632-mediated differences in neurite outgrowth.

Lastly, we are the first to study Y-27632 in a more physiologically-relevant and novel 3-D model, human cortical organoids (‘mini-brains’), to better recapitulate neurodevelopment of the human brain. Specifically, we investigate the effects of Y-27632-mediated ROCK inhibition on excitatory synapse formation in this hIPSC-derived ‘mini-brain’ model.

A.

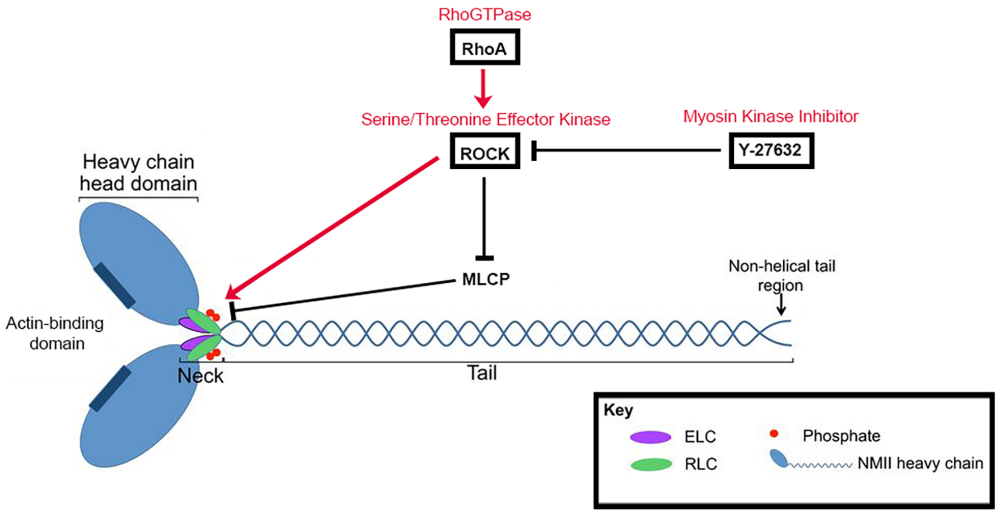

B.

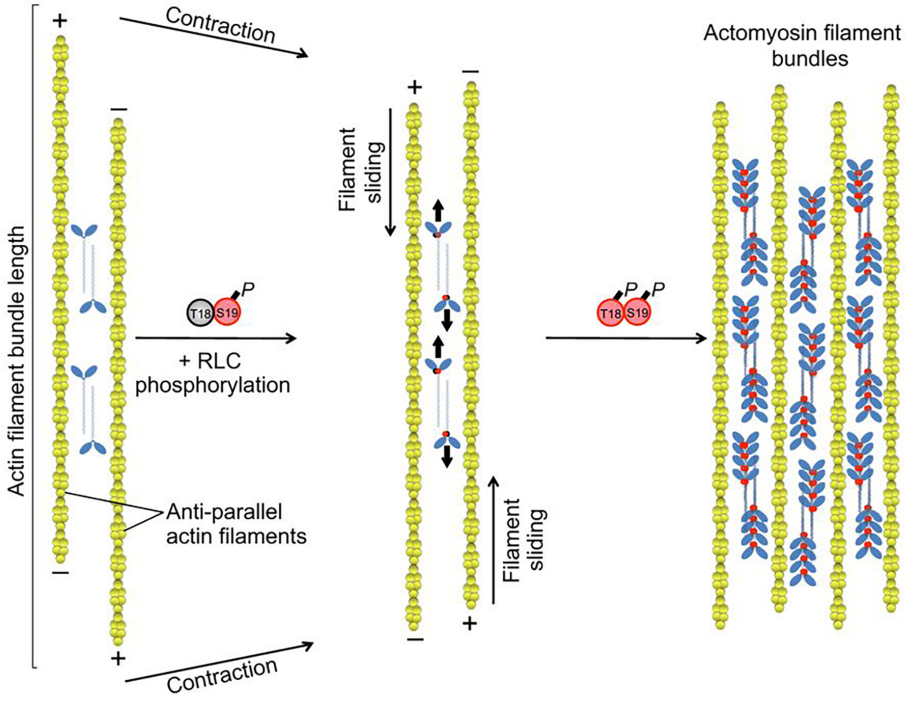

Diagram 4. Inhibition of NM-II Activation Causes Less Actomyosin Filament Bundle Formation. (A) ROCK phosphorylates the RLC of NM-II, forming pRLC, causing activation of NM-II. Therefore, Y-27632 mediated ROCK inhibition leads to less pRLC and NM-II activity. The myosin head of NM-II moves toward the barbed(+) ends of anti-parallel actin filaments, contracting the filaments towards their pointed(-) ends. This forms actomyosin filament bundles capable of contractile forces. Thus, Y-27632-mediated ROCK inhibition inhibits NM-II activation, leading to the formation of less actomyosin filament bundles. (Figure adapted from Newell-Litwa et al. [40], legend modified)

Hypotheses

Hypothesis #1 (2-D): Y-27632-mediated ROCK inhibition increases neural complexity in hIPSC-derived neurons. In particular, Y-27632 promotes the formation of more neurites that are longer in length with increased branching.

Hypothesis #2 (3-D): Y-27632-mediated ROCK inhibition increases neural complexity in hIPSC-derived 'mini-brains' as in 2-D hIPSC-derived neurons. Furthermore, Y-27632 reduces the formation of mature mushroom-shaped spines, resulting in decreased excitatory synapses.

CHAPTER 2: MATERIALS AND METHODS

Cell Lines

The four neurotypic control skin fibroblast cell lines BJ (control cell line #1), 9319 (control cell line #2), WTC-11 (control cell line #3), and 7545 (control cell line #4) were reprogrammed into human-induced pluripotent stem cells (hIPSCs) with the addition of Yamanaka transcription factors Oct3/4, Sox2, Klf4, and c-Myc [50] using the Invitrogen™ CytoTune™-iPS 2.0 Sendai Reprogramming Kit. hIPSCs from control cell lines #1 and #2 were generated by Kristen Brennand in the lab of Dr. Fred Gage at the Salk Institute, while hIPSCs from control cell line #4 were generated in the lab of Dr. McConnell at the University of Virginia School of Medicine. Moreover, hIPSCs from control cell line #3 were generated in the lab of Dr. Bruce Conklin at the Gladstone Institute of Cardiovascular Disease. Beta actin (ActB) of control cell line #3 hIPSCs was later endogenously tagged with monomeric enhanced green fluorescent protein (mEGFP) using CRISPR/Cas9 technology at the Allen Institute for Cell Science, creating ActB mEGFP hIPSCs. Note, control cell lines #1 and #2 hIPSCs were obtained under a material transfer agreement (MTA) with Kristen Brennand and the Salk Institute, while control cell lines #3 and #4 hIPSCs were obtained under an MTA with the Coriell Institute.

NPC Culture

Neural progenitor cells (NPCs) were generated from control cell lines #1, #2, and #3 hIPSCs through an embryoid body protocol as described by Brennand et al. [5]. In summary, 1mL/well of PluriSTEM™ Dispase-II Solution was used to dissociate hIPSCs

from Corning™ Costar™ ultra-low attachment 6-well plastic plates to form floating embryoid bodies. Floating embryoid bodies were then cultured in 2mL/well of Gibco® Essential 6™ Medium for one day. The next day media was switched to 2mL/well of Gibco® Dulbecco's Modified Eagle Medium/Nutrient Mixture F-12 (DMEM/F-12) + GlutaMAX supplemented with 1% of Gibco® N-2, 2% of Gibco® B-27™ without vitamin A, 10μM of StemMACS™ SB431542, and 100nM of STEMCELL™ TECHNOLOGIES LDN193189 inside a tissue culture incubator set at 5% CO_2 and 37ºC. After 7 days in culture, embryoid bodies were plated onto Sigma Aldrich® Poly-L-Ornithine (pORN) and Corning™ laminin-coated Bio-One® CELLSTAR® 6-well plastic tissue culture plates. Embryoid bodies were then cultured in the same media for an additional 7 days until neural rosettes formed. Lastly, 1mL/well of STEMdiff™ Neural Rosette Selection Reagent was used to dissociate neural rosettes, forming NPCs. Note, control cell lines #1 and #2 NPCs were generated by Kristen Brennand in the lab of Dr. Fred Gage at the Salk Institute, while control cell line #3 NPCs were generated by lab technician Brenna Kirk in the lab of Dr. Litwa at the Brody School of Medicine.

NPCs were grown on Sigma Aldrich® pORN and Corning™ laminin-coated Bio-One® CELLSTAR® 6-well plastic tissue culture plates for the first four passages inside a tissue culture incubator set at 5% CO_2 and 37ºC in 2mL/well of NPC media, which consists of Gibco® DMEM/F-12 + GlutaMAX, 1% of Gibco® N-2, 2% of Gibco® B-27™ without vitamin A, 1μg/mL of Corning™ laminin, and 20ng/mL of PeproTech® basic fibroblast growth factor (bFGF). After four passages, NPCs were grown on Corning™ matrigel-coated Greiner Bio-One® CELLSTAR® 6-well plastic tissue culture plates instead. NPC media was replaced every other day and cells were grown to a confluency of no more

than 80% before subsequent cell splitting. During cell passaging, 500µL/well of StemPro® Accutase® from Gibco® by Life Technologies™ was used to lift cells from plates. NPCs used for experiments had a passage number below 15 and were at least 90% viable as determined by the Countess® Automated Cell Counter from Invitrogen™.

Differentiation of hIPSC-derived NPCs into Neurons

Following overnight plating, 200,000 NPCs per well were differentiated at 37ºC and 5% CO_2 inside a tissue culture incubator on Sigma Aldrich® pORN and Corning™ laminin coated Bio-One® CELLSTAR® 6-well plastic tissue culture plates for 24 hours in 2mL/well of neural differentiation media, consisting of Gibco® DMEM/F-12 + GlutaMAX, 1% of Gibco® N-2, 2% of Gibco® B-27™ with vitamin A, 20ng/mL of Shenandoah Biotechnology Inc™ BDNF, 20ng/mL of Shenandoah Biotechnology Inc™ glial cell-derived neurotrophic factor (GDNF), 400uM of Sigma Aldrich® cyclic adenosine monophosphate (cAMP), and 200nM of ascorbic acid from Fisher Scientific supplemented with 0µM, 5µM, 10µM, 25µM, or 50µM of Y-27632. Experiments were completed with control cell lines #1, #2, and #3 NPCs. Note for time lapse experiments, 100,000 NPCs per well were differentiated on Sigma Aldrich® pORN and Corning™ laminin coated MatTek® 6-well glass bottom tissue culture plates at 37ºC and 5% CO_2 inside the ZEISS LSM 700 Confocal onstage incubator. Time-lapse experiments were completed with control cell line #3 NPCs only, since the endogenous GFP enabled monitoring of neurite and actin dynamics by fluorescent microscopy.

‘Mini-brain’ Culture

Human cortical organoids (‘mini-brains’) were generated from control cell line #4 hIPSCs by lab technician Brenna Kirk in the lab of Dr. Litwa at the Brody School of Medicine as described by Pasca et al. [41]. In summary, hiPSCs were added to Corning™ Costar™ ultra-low attachment 6-well plastic plates in 4mL/well of Gibco® Knockout™ Serum Replacement based media, which caused hIPSCs to aggregate into spheroids. 5μM of Dorsomorphin from BioVision Incorporated and 10μM of StemMACS™ SB431542 by Miltenyi Biotec were then added to the media to inhibit bone morphogenetic protein (BMP) and transforming growth factor beta (TGF-ß) signaling pathways, leading to neural induction. After 6 days, the suspended spheroids were moved to 2mL/well of Gibco® Neurobasal™- A media supplemented with 2% of Gibco® B-27™ without vitamin A, 20ng/mL of PeproTech® bFGF, and 20ng/mL of PeproTech® epidermal growth factor (EGF). Supplemented neurobasal media was changed every day for 10 days and every other day for the following 9 days. On day 25, bFGF and EGF were replaced with 20ng/mL of brain-derived neurotrophic factor (BDNF) and 20ng/mL of neurotrophic factor 3 (NT3) from Shenandoah Biotechnology Inc™ to promote neural differentiation of NPCs within the ‘mini-brain.’ Note, media was changed every other day for 18 days. 4mL/well of non-supplemented Gibco® Neurobasal™- A media was used from day 43 onwards, changing media every 4 days. After 89 days, ‘mini-brains’ were either treated with 10μM of the Rho-Kinase (ROCK) inhibitor Y-27632 from Selleck for 24 hours or left untreated. ‘Mini-brains’ were then harvested for protein or fixed for immunofluorescence staining on day 90. Note, ‘mini-

brains' were cultured inside a tissue culture incubator set at 5% CO_2 and 37ºC for the entire process. For a schematic of 'mini-brain' generation, please see Diagram 5.

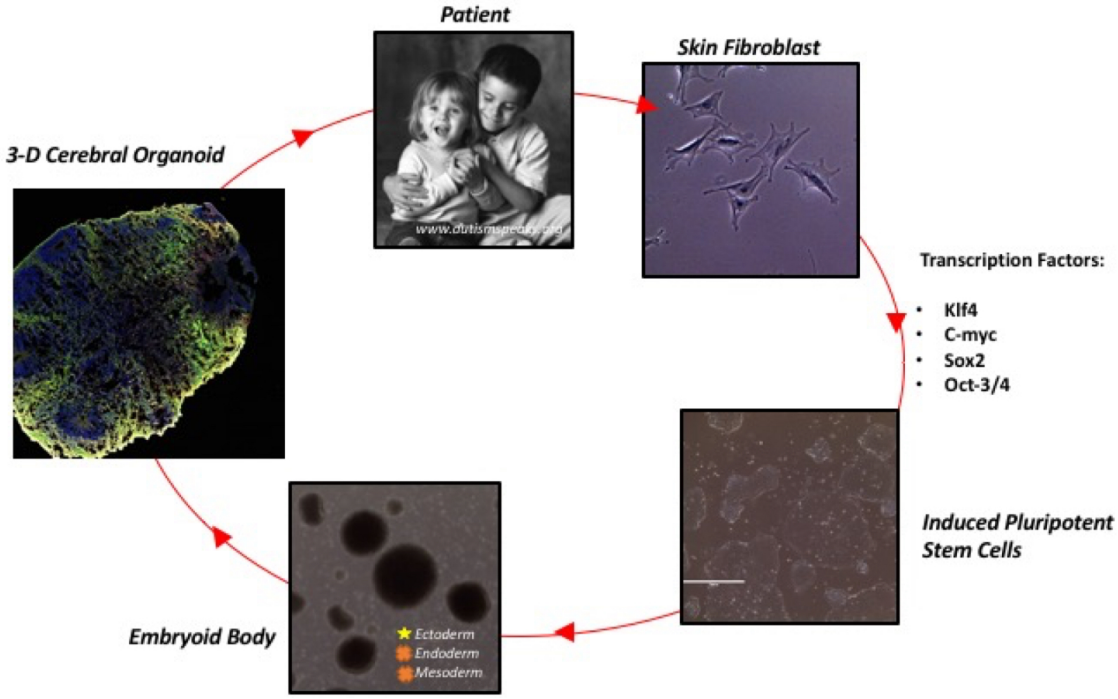

Diagram 5. Generation of hIPSC-derived 'Mini-brains'. Skin fibroblasts samples from neurotypic control patients were reprogrammed into induced pluripotent stem cells with the addition of Yamanaka transcription factors. Induced pluripotent stem cells then aggregated to form embryoid bodies. Lastly, the ectoderm of embryoid bodies were selected for and differentiated into 3-D cerebral organoids.

Immunohistochemistry

hIPSC-derived neurons were fixed after 24 hours of neural differentiation for 20 minutes at room temperature with 4% formaldehyde with 4% sucrose in 1X phosphate-buffered saline (PBS). Fixed cells were then permeabilized for 2 minutes at room temperature with 0.1% Triton X-100 in 1X PBS. Next, cells were blocked with 5% goat serum in 1X PBS for 30 minutes. Blocked cells were then incubated in diluted primary antibodies in 2% goat serum overnight at 4ºC. After overnight primary antibody incubation, cells were incubated in diluted Alexa Fluor® secondary antibodies in 2% goat serum in the dark for one hour at room temperature. For more information about primary and secondary antibodies used, please see Tables 1 and 2 in Appendix A. Lastly, the nuclei of cells were stained using DAPI staining solution from GeneTex® for 10 minutes at room temperature.

'Mini-brains' were fixed with 4% formaldehyde in 1X PBS at 4ºC overnight. The following day, fixed 'mini-brains' were placed in 30% sucrose in 1X PBS at 4ºC overnight. Joani Zary, a research specialist in the Department of Anatomy and Cell Biology at the Brody School of Medicine, then embedded the 'mini-brains' into a disposable base mold from Simport Scientific Inc. with O.C.T. compound from Sakura Finetek USA Inc. and froze them with dry ice/2-methyl butane slush from Fisher Scientific. Subsequently, Joani sectioned the 'mini-brains' 10µm thick on a Richard-Allan Scientific cryostat. Finally, she thaw mounted sections onto 2% 3-Aminopropyl Triethoxysilane treated slides. Slides of cryosectioned 'mini-brains' were assembled onto cover plates with 0.2% Triton X-100 in 1X PBS and placed into a Sequenza rack. Next, 'mini-brains' were blocked with

120µL/slide of 5% goat serum in 1X PBS for 30 minutes. Blocked mini-brains were then incubated in 120µL/slide of various primary antibodies in 2% goat serum overnight at 4ºC. After overnight primary antibody incubation, slides were incubated in 120µL/slide of diluted Alexa Fluor® secondary antibodies in 2% goat serum in the dark for one hour at room temperature. For more information about primary antibodies and secondary antibodies used, please see Tables 1 and 2 in Appendix A. Lastly, No. 1 Fisherbrand® cover glasses were affixed to slides with Fluoro-Gell II with DAPI from Electron Microscopy Sciences, which stained for nuclei of 'mini-brains.'

Imaging Analysis

Representative images were taken of fixed hIPSC-derived neurons using DAPI and Invitrogen Texas Red light cubes in the EVOS™ FL Auto 2 at 20X total magnification. For quantification, 100 fields of each well of immunofluorescently stained hIPSC-derived neurons were imaged at 10X total magnification and simultaneously analyzed using the Neuronal Profiling Assay V4.2 of the Thermo Scientific™ CellInsight™ CX5 High Content Screening Platform. In Y-27632-mediated ROCK inhibiton confirmation experiments, cell features cellbodyspotavginten and neuritespotavginten were selected to measure the average intensity of both phosphorylated (S19/S20) myosin light chain/regulatory light chain (pRLC) and myosin light chain/regulatory light chain (RLC) within neurites and cell bodies of neurons. Afterwards, the average neurite intensity of pRLC within each neuron was divided by the average neurite intensity of RLC. Likewise, the cell body intensity of pRLC within each neuron was divided by the cell body intensity of RLC. Additionally, the cell features neuritetotalcount, neuriteavglength, and branchpointavgcount were utilized

to measure total number, average length, and average number of branch points of neurites within neurons.

For time lapse experiments, actin dynamics within differentiating control cell line #3 NPCs were recorded using the 488nm laser of the ZEISS LSM 700 confocal at 20X total magnification. Two locations within each treatment group well were imaged every 10 minutes for 20 hours for a total of 120 images per location and 240 images per treatment group. The images were then examined to determine how long five random neurites per location (10 different neurites per treatment group) protruded before beginning to retract, referred to as neurite persistence. Furthermore, the measuring tool of ImageJ 1.51 j8 was utilized to measure the length of five random neurites per location (10 different neurites per treatment group) throughout the entirety of neurite protrusion and retraction events. Instantaneous protrusion and retraction rates were then calculated using the change of neurite length divided by the time elapsed between each frame. For example, a 10μm increase in neurite length between t=10min and t=20 min would be an average instantaneous protrusion rate of 1μm/min or 60μm/hr. A 10μm decrease in neurite length between t=10 min and t=20 min would be an average instantaneous retraction rate of 1μm/min or 60μm/hr.

For ‘mini-brain’ analyses, immunofluorescently stained ‘mini-brains’ were imaged using 405nm, 488nm, 555nm, and 639nm lasers of the ZEISS LSM 700 confocal at 20X total magnification. The area of various proteins was then analyzed within ten circular regions of 100μm in diameter around the edge of each ‘mini-brain.’

Statistical Analysis

Statistical analyses were performed using SigmaPlot 13.0. For hIPSC-derived neuron analyses, data was first tested for normality using Kolmogorov-Smirnov tests. After rejection of the null hypothesis, non-parametric data was analyzed using Kruskal-Wallis tests, a one-way analysis of variance (ANOVA) based on ranks. Following rejection of the Kruskal-Wallis null hypothesis, a pairwise multiple comparison post hoc Dunn's tests were used to test for statistically significant differences among treatment groups.

For 'mini-brain' analyses, data was first tested for normality using Shapiro-Wilk tests. After rejection of the null hypothesis, non-parametric data was analyzed using Mann-Whitney Rank Sum tests to test for statistical significance. Error bars represent standard error in all graphs. $*p < 0.05$ $**p < 0.001$

CHAPTER 3: RESULTS

Y-27632-mediated ROCK Inhibition Decreases RLC Phosphorylation (2D)

To confirm the effectiveness of the Rho-Kinase (ROCK) inhibitor Y-27632 in human-induced pluripotent stem cell (hIPSC)-derived neurons, control cell line #2 human neurons were treated with Y-27632 for the first 24 hours of differentiation, and were then fixed and stained with DAPI to identify nuclei, β-III Tubulin to identify neurons, phosphorylated (S19/S20) myosin light chain/regulatory Light Chain (pRLC) to identify phosphorylation and activation of the ROCK substrate non-muscle myosin II (NM-II), and myosin light chain/regulatory light chain (RLC) to identify both phosphorylated (active) and non-phosphorylated (inactive) NM-II. Given the fact ROCK phosphorylates NM-II and Y-27632 is a ROCK inhibitor [Diagram 4A], we expect to see a Y-27632 dose-dependent decrease in the ratio of pRLC intensity (active NM-II) normalized to RLC intensity (active and inactive NM-II) in hIPSC-derived neurons.

Normalized to the control treatment group, the average ratio of pRLC to RLC average neurite intensity in neurons significantly decreased by 2.18%, 7.23%, 11.06%, and 20.17% in 5μM, 10μM, 25μM, and 50μM Y-27632 24-hour treatment groups, respectively (Figure 1A). Similarly, the average ratio of pRLC to RLC in cell bodies of neurons, normalized to the control group, significantly decreased by 2.14%, 10.78%, 7.70%, and 22.20% in 5μM, 10μM, 25μM, and 50μM Y-27632 24-hour treatment groups, respectively (Figure 1B). As expected, these results reveal a Y-27632 dose-dependent inhibition of ROCK and its phosphorylation and subsequent activation of NM-II. Therefore, the effectiveness of Y-27632 in hIPSC-derived neurons is confirmed.

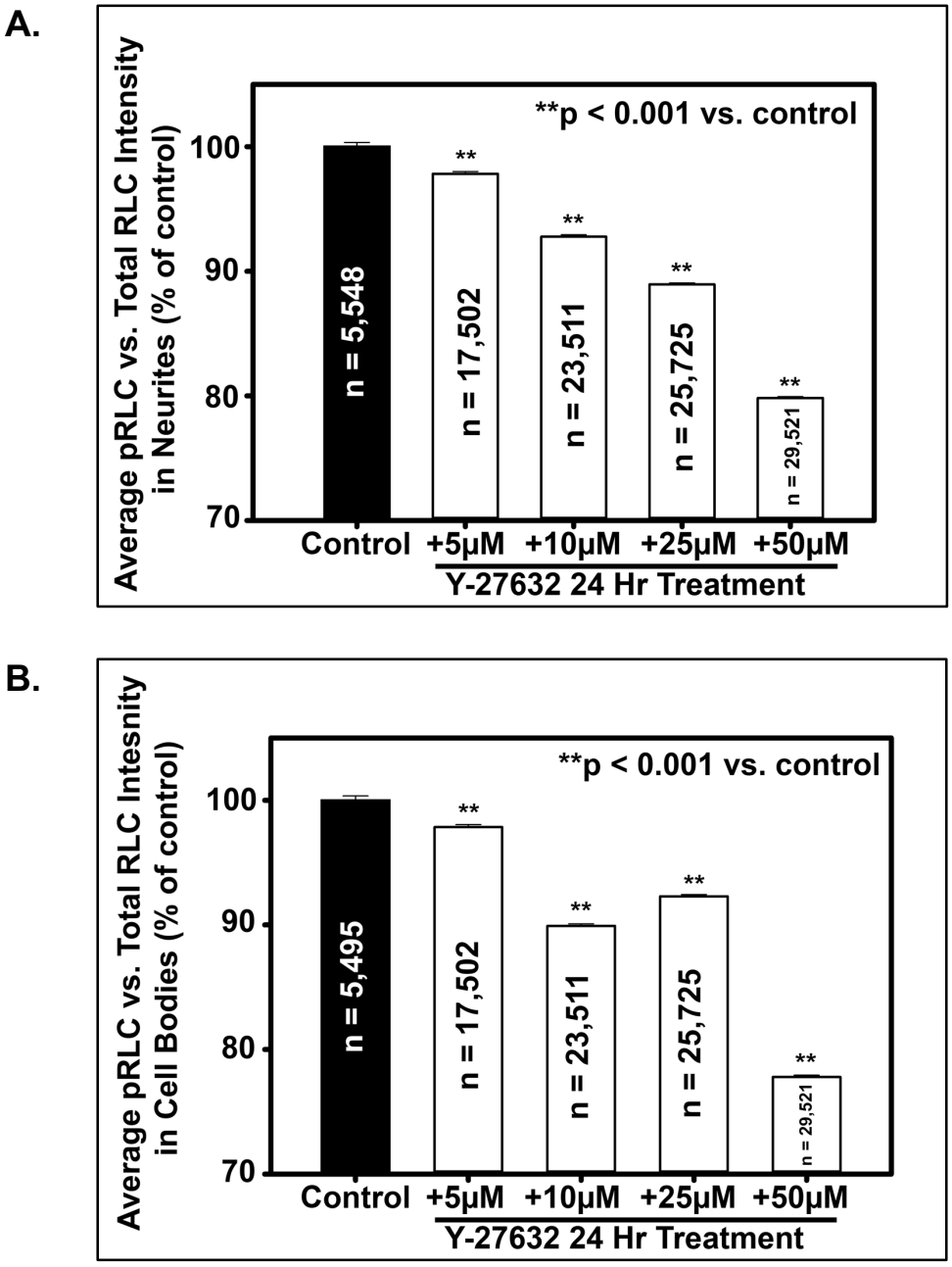

Figure 1. Y-27632 Significantly Decreases ROCK-mediated NM-II Activation. (A) Average pRLC vs. total RLC intensity, represented as percent of control, in neurites of control cell line #2 hIPSC-derived neurons following either 5μM, 10μM, 25μM, or 50μM Y-27632 treatment and 24-hour neural differentiation. (B) Average pRLC vs. total RLC intensity, represented as percent of control, in cell bodies of control cell line #2 hIPSC-derived neurons following either 5μM, 10μM, 25μM, or 50μM Y-27632 treatment and 24-hour neural differentiation. (See Table 7 in Appendix C for multiple comparison p values) (n values provided in figure, ** $p < 0.001$) Experiment repeated twice.

Y-27632 Promotes Neurite Formation, Elongation, and Branching (2-D)

Human-induced (hIPSC)-derived neurons were utilized to further characterize the effects of Y-27632-mediated ROCK inhibition on neurite formation. Control cell lines #1, #2, and #3 human neurons were treated with Y-27632 for the first 24 hours of differentiation, and were then fixed and stained with β-III Tubulin to identify neurons, and DAPI to identify nuclei. Y-27632 treatment groups for all three cell lines visually appear to have more neuronal cells with increased neurite length and branching as compared to the control (Figure 2A, 2B, 2C).

Normalized to the control, the average percent of neuronal cells in control cell line #1 hIPSC-derived neurons significantly increased by 33.71%, 42.13%, 33.86%, and 37.85% in 5μM, 10μM, 25μM, and 50μM Y-27632 treatment groups, respectively (Figure 3A). Normalized to the control, the average percent of neuronal cells in control cell line #2 hIPSC-derived neurons significantly increased by 41.69%, 68.74%, 66.35%, and 70.47% in 5μM, 10μM, 25μM, and 50μM Y-27632 treatment groups, respectively (Figure 3B). Normalized to the control, the average percent of neuronal cells in control cell line #3 hIPSC-derived neurons significantly increased by 15.81%, 18.54%, 19.29%, and 18.66% in 5μM, 10μM, 25μM, and 50μM Y-27632 treatment groups, respectively (Figure 3C). These results reveal a trend of a Y-27632 dose-dependent increase in average percent of neuronal cells until plateauing at 10μM in all three cell lines.

Furthermore, Y-27632 increased the number of neurites in these neuronal cells. Normalized to the control, the average number of neurites per neuron in control cell line #1 hIPSC-derived neurons significantly increased by 7.82% and 6.68% in 10μM and

50μM Y-27632 treatment groups, respectively (Figure 4A). Moreover, normalized to the control, the average number of neurites per neuron in control cell line #1 hIPSC-derived neurons insignificantly increased by 4.88% and 4.26% in 5μM and 25μM Y-27632 treatment groups, respectively (Figure 4A). Normalized to the control, the average number of neurites per neuron in control cell line #2 hIPSC-derived neurons significantly increased by 5.13%, 11.63%, 11.60%, and 13.29% in 5μM, 10μM, 25μM, and 50μM Y-27632 treatment groups, respectively (Figure 4B). Normalized to the control, the average number of neurites per neuron in control cell line #3 hIPSC-derived neurons significantly increased by 9.18%, 10.76%, 9.44%, and 12.61% in 5μM, 10μM, 25μM, and 50μM Y-27632 treatment groups, respectively (Figure 4C). With the exception of 5μM and 25μM Y-27632 treatment groups of control cell line #1 hIPSC-derived neurons, these results reveal a trend of a Y-27632 dose-dependent increase in average number of neurites per neuron until plateauing at 10μM in all three cell lines.

In addition to increasing neurite formation, Y-27632 also increased neurite length. Normalized to the control, the average neurite length of control cell line #1 hIPSC-derived neurons significantly increased by 17.85%, 30.71%, 26.95%, and 32.54% in 5μM, 10μM, 25μM, and 50μM Y-27632 treatment groups, respectively (Figure 5A). Normalized to the control, the average neurite length of control cell line #2 hIPSC-derived neurons significantly increased by 23.00%, 39.00%, 37.64%, and 43.67% in 5μM, 10μM, 25μM, and 50μM Y-27632 treatment groups, respectively (Figure 5B). Normalized to the control, the average neurite length of control cell line #3 hIPSC-derived neurons significantly increased by 20.98%, 29.06%, 33.41%, and 39.92%% in 5μM, 10μM, 25μM, and 50μM Y-27632 treatment groups, respectively (Figure 5C). These results reveal a trend of a Y-

27632 dose-dependent increase in neurite length that plateaued at 10μM in all three cell lines.

The significant increase in average percent of neuronal cells, number of neurites per neuron, and neurite length exhibited in hIPSC-derived neurons can in part be explained by the same molecular mechanism. ROCK1 and ROCK2 phosphorylate and activate NM-II, leading to the formation of actomyosin filament bundles capable of generating contractile forces [Diagram 4]. Moreover, ROCK1 and ROCK2 further promote NM-II activation and actomyosin filament bundle formation by inhibiting MLCP [Diagram 4]. Since Y-27632 inhibits ROCK-mediated activation of NM-II (Figure 1), less actomyosin filament bundles are formed. Consequently, Y-27632 treated hIPSC-derived neurons may produce weaker NM-II-driven contractile forces that would typically cause a neurite precursor to retract towards the cell body. Instead more neurite precursors may persist (Figure 7, 8A), which possibly explains the Y-27632-mediated increase in average percent of neuronal cells and average number of neurites per neuron. Furthermore, ROCK2 is also known to inhibit Rac-driven actin polymerization [39]. Hence, neurites of Y-27632 treated hIPSC-derived neurons may express increased Rac1 activity leading to increased actin polymerization. Increased actin polymerization in combination with less NM-II-driven contractility via ROCK1 and ROCK2 inhibition, causes neurite precursors of Y-27632 treated hIPSC-derived neurons to become significantly longer.

Förster resonance energy transfer (FRET) can be used to further support these hypotheses by measuring the potential decrease in NM-II forces associated with Y-27632 treatment. FRET or a Rac and p21-activated Kinase (PAK) pulldown assay could also

be used to directly measure the potential increase in Rac activity. Additionally, western blots can be utilized to measure the potential differences in expression of proteins within the Rac-driven actin polymerization pathway.

Y-27632 further increased neuronal complexity by increasing the number of branch points (the point where a neurite diverges into two). A trend of a Y-27632 dose-dependent increase in average number of branch points was observed in all three cell lines until plateauing around 10μM. Normalized to the control treatment group, the average number of branch points in control cell line #1 hIPSC-derived neurons significantly increased by 58.86%, 75.36%, 59.09%, and 86.56% in 5μM, 10μM, 25μM, and 50μM Y-27632 treatment groups, respectively (Figure 6A). Normalized to the control treatment group, the average number of branch points in control cell line #2 hIPSC-derived neurons significantly increased by 68.10%, 139.32%, 146.77%, and 164.51% in 5μM, 10μM, 25μM, and 50μM Y-27632 treatment groups, respectively (Figure 6B). Normalized to the control treatment group, the average number of branch points in control cell line #3 hIPSC-derived neurons significantly increased by 52.09%, 70.48%, 73.10%, and 86.43% in 5μM, 10μM, 25μM, and 50μM Y-27632 treatment groups, respectively (Figure 6C).

Future experiments are needed to determine the molecular mechanism of this significant increase. It is possible that Y-27632 may indirectly cause increased Rac1-mediated ARP2/3 activity by increasing the activation of Wiskott–Aldrich Syndrome protein (WASP)-family proteins for example, leading to increased nucleation and branching of more daughter filaments from mother filaments.

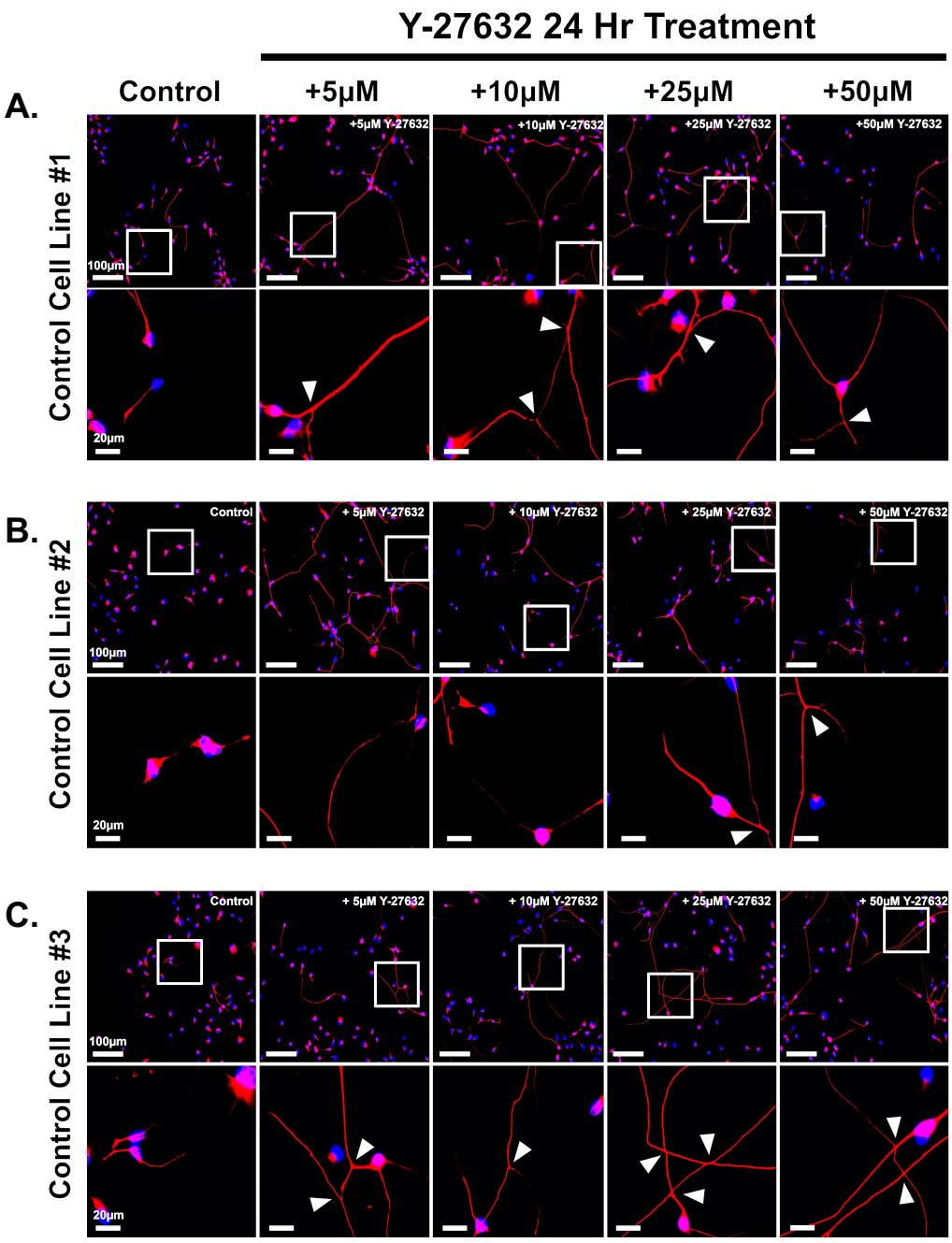

Figure 2. **hIPSC-derived Neurons.** Representative images of three different hIPSC-derived neural progenitor cell lines differentiated for 24 hours following either 0μM (control), 5μM, 10μM, 25μM, or 50μM Y-27632 treatment. Cells were stained for neurons (β-III Tubulin, red) and nuclei (DAPI, blue). Insets included below each image with branch points identified (see white arrowheads). (A) Control cell line #1 hIPSC-derived neurons. (B) Control cell line #2 hIPSC-derived neurons. (C) Control cell line #3 hIPSC-derived neurons. Experiment repeated three times.

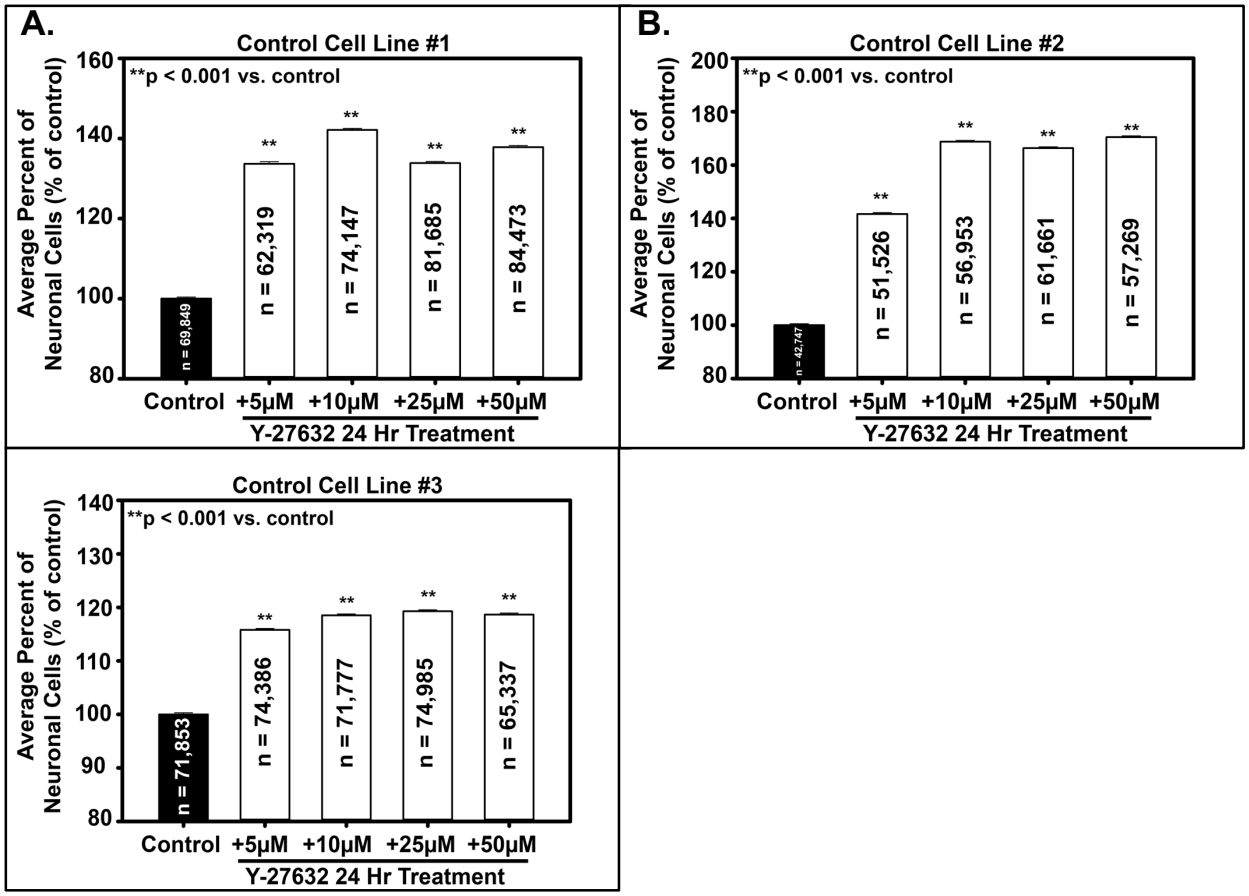

Figure 3. Y-27632 Significantly Increases Percent of Neuronal Cells. The average percent of neuronal cells in hIPSC-derived neurons that were treated with either 5μM, 10μM, 25μM, or 50μM of Y-27632 and differentiated for 24 hours. (A) Control cell line #1 hIPSC-derived neurons. (B) Control cell line #2 hIPSC-derived neurons. (C) Control cell line #3 mEGFP hIPSC-derived neurons. (n values provided in bar charts) (See Table 3 in Appendix B for absolute averages and Table 8 in Appendix C for multiple comparison p values) (* $p < 0.05$, ** $p < 0.001$) Experiment repeated three times.

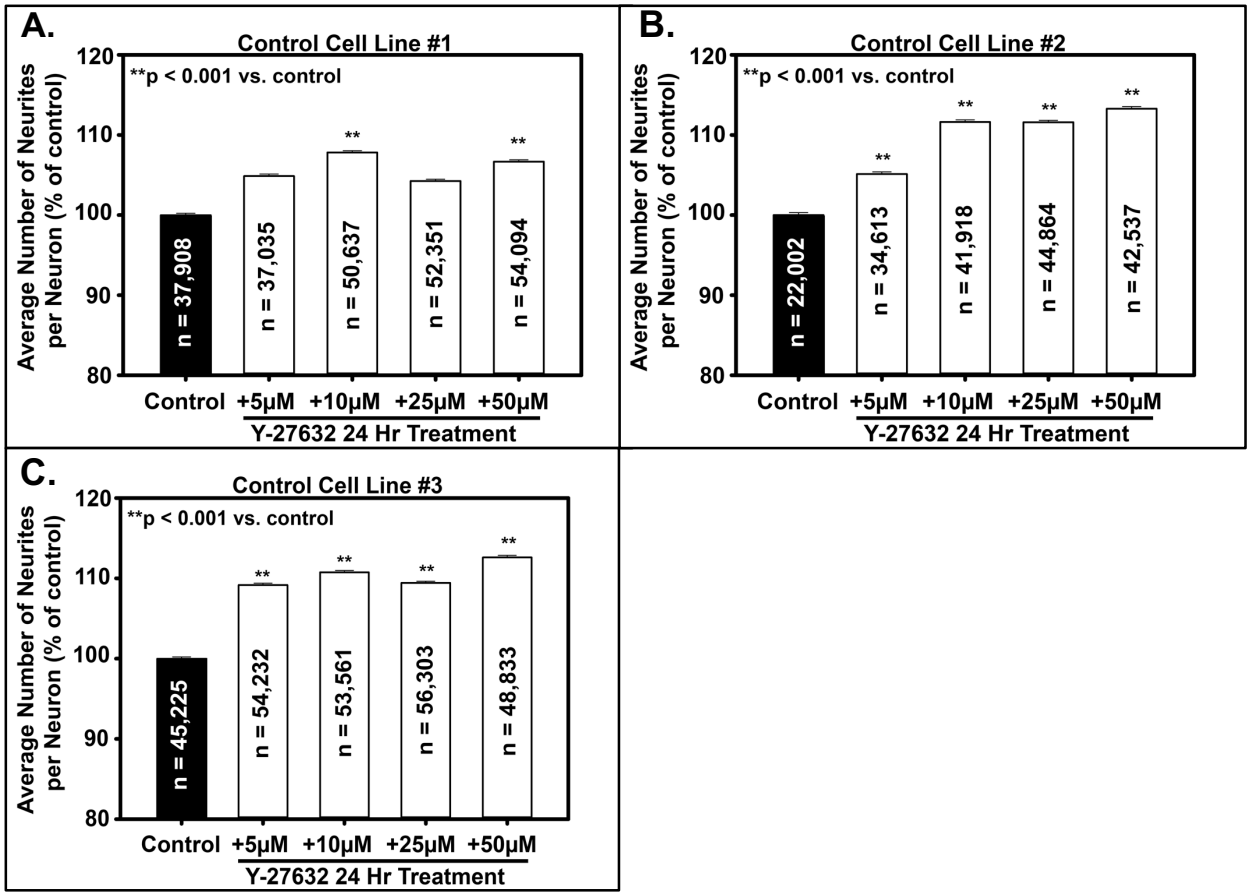

Figure 4. Y-27632 Significantly Increases Number of Neurites per Neuron. The average number of neurites, represented as percent of control, in hIPSC-derived neurons that were treated with either 5μM, 10μM, 25μM, or 50μM of Y-27632 and differentiated for 24 hours. (A) Control cell line #1 hIPSC-derived neurons. (B) Control cell line #2 hIPSC-derived neurons. (C) Control cell line #3 hIPSC-derived neurons. (n values provided in bar charts) (See Table 4 in Appendix B for absolute averages and Table 9 in Appendix C for multiple comparison p values) (* $p < 0.05$, ** $p < 0.001$) Experiment repeated three times.

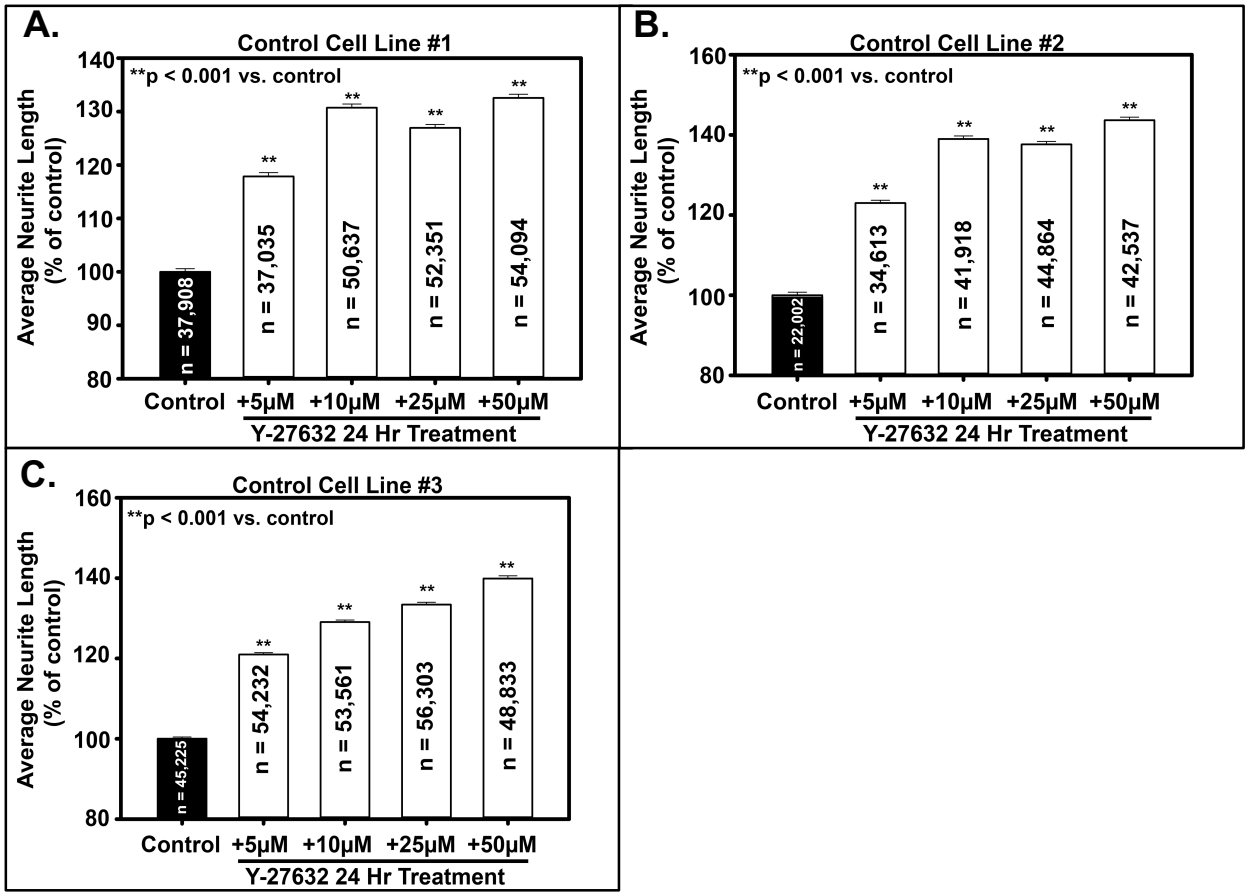

Figure 5. Y-27632 Significantly Increases Neurite Length. All three graphs represent the average neurite length in hIPSC-derived NPCs following treatment with either 0μM (control), 5μM, 10μM, 25μM, or 50μM of Y-27632 and a 24 hour period of differentiation. (A) Control cell line #1 hIPSC-derived neurons. (B) Control cell line #2 hIPSC-derived neurons. (C) Control cell line #3 hIPSC-derived neurons. (n values provided in tables inside of graphs) (See Table 5 in Appendix B for absolute averages and Table 10 in Appendix C for multiple comparison p values) (** $p < 0.001$) Experiment repreated three times.

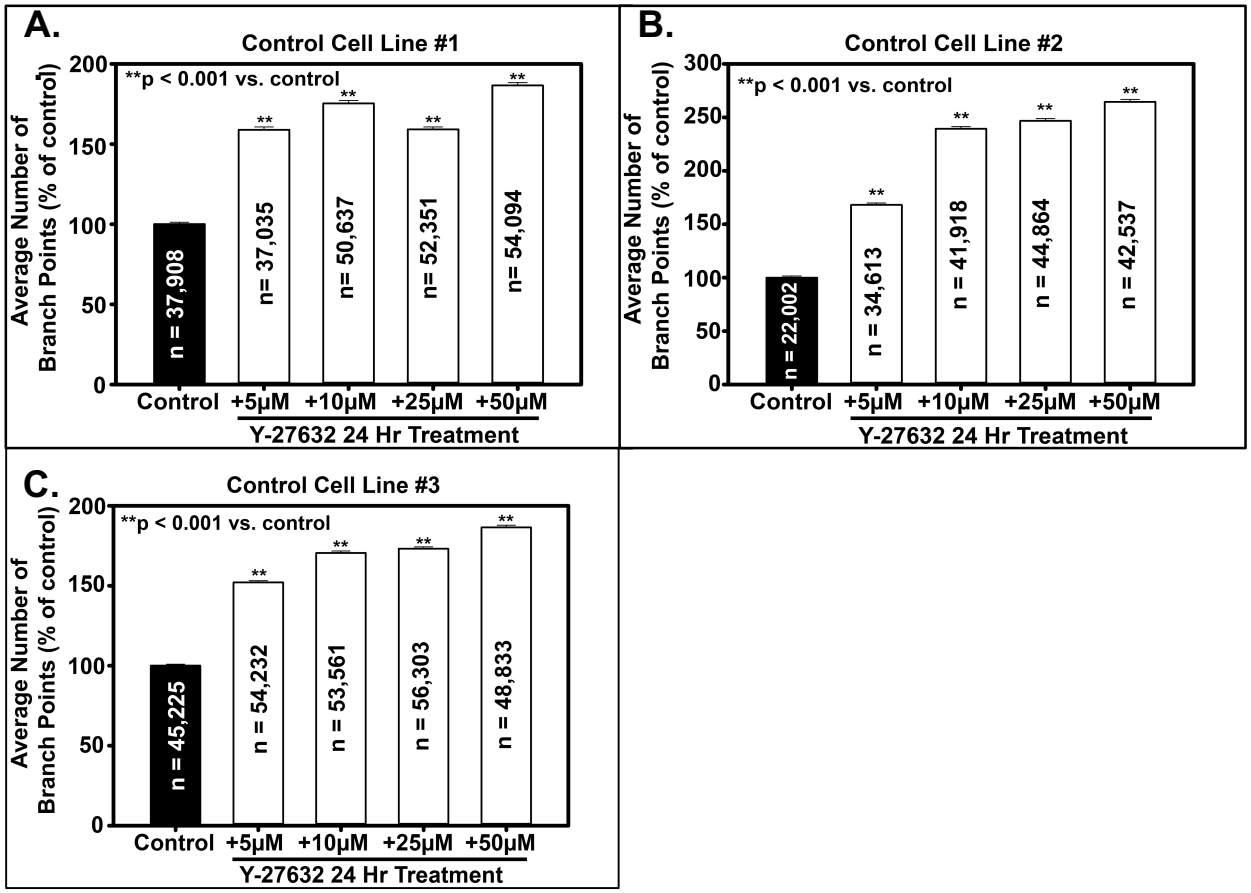

Figure 6. Y-27632 Significantly Increases Number of Branch Points. The average number of branch points, represented as percent of control, in hIPSC-derived neurons that were treated with either 5μM, 10μM, 25μM, or 50μM of Y-27632 and differentiated for 24 hours. (A) Control cell line #1 hIPSC-derived neurons. (B) Control cell line #2 hIPSC-derived neurons. (C) Control cell line #3 hIPSC-derived neurons. (n values provided in bar charts) (See Table 6 in Appendix B for absolute averages and Table 11 in Appendix C for multiple comparison p values) (* $p < 0.05$, ** $p < 0.001$) Experiment repeated three times.

Y-27632 Alters Neurite Dynamics (2-D)

To further understand the neurite dynamics underlying the observed increase in neuronal complexity as demonstrated by increased neurite number, length, and branch points in hIPSC-derived neurons, hIPSC-derived NPCs from control cell line #3 were imaged during neural differentiation. ActB of this control hIPSC-derived NPC line was previously gene-edited to express mEGFP, making this cell line ideal for following live actin dynamics within neurites and cell bodies during neural differentiation. Fluorescently labeling live cells, especially neurons, can be very troublesome due to cytotoxicity effects and low transfection efficiency. Thus, this cell line provides us with an invaluable tool to further investigate possibly altered actin dynamics within neurites of differentiating Y-27632 treated NPCs.

Still frames of time-lapse movies demonstrate increased neurite elongation in Y-27632 treated differentiating NPCs compared to the control (Figure 7). Moreover, the dynamics of neurites in the control group appeared to be much more erratic as compared to neurites of Y-27632 treated groups. Specifically, the neurites seemed to protrude and retract much faster. Neurites of 5μM and 10μM Y-27632 treated groups on the other hand appeared to protrude at a slower rate and persist for much longer. Furthermore, when and if the neurites did retract, they did so at a seemingly slower rate.

Control cell line #3 hIPSC-derived neurons treated with neural differentiation media only (control) exhibited an average neurite persistence (how long a neurite protrudes before beginning to retract) of 79min compared to 177min in 5μM Y-27632 treated neurons and 206min in 10μM Y-27632 treated neurons (Figure 8A). To further delineate

this Y-27632-mediated increase in neurite persistence, time-lapse movies were further analyzed for rates of neurite protrusion and retraction. Neurites of control cell line #3 hIPSC-derived neurons treated with neural differentiation media only (control) exhibited an average instantaneous protrusion rate of 34μm/hr compared to 21μm/hr in 5μM Y-27632 treated neurons and 20μm/hr in 10μM Y-27632 treated neurons (Figure 8B). This reveals a significant decrease in neurite protrusion rates of Y-27632 treated hIPSC-derived neurons. However, the Y-27632 treatment groups are not significantly different from one another. Control cell line #3 hIPSC-derived neurons treated with neural differentiation media only (control) exhibited an average instantaneous retraction rate of 50μm/hr compared to 28μm/hr in 5μM Y-27632 treated neurons and 24μm/hr in 10μM Y-27632 treated neurons (Figure 8C). This reveals a significant Y-27632 dose-dependent decrease in neurite retraction rates.

These results support the proposed molecular mechanism underlying the observed significant increase in neurite number and neurite length of Y-27632 treated hIPSC-derived neurons. In summary, Y-27632-mediated ROCK inhibition may decrease NM-II-driven contractility and increase Rac-driven actin polymerization in hIPSC-derived neurons. Decreased NM-II-driven contractility is supported by the observation of decreased neurite retraction rates in Y-27632 treated hIPSC-derived neurons. A stronger NM-II-driven force would generate much faster neurite retraction rates similar to those observed in control neurons. Also, decreased NM-II-driven contractility may generate forces too weak to shorten some neurites more than they have lengthened via increased Rac-driven actin polymerization. This may give rise to neurite elongation and increased neurite persistence. Together, these results provide support for decreased NM-II driven

contractility via decreased phosphorylation of RLC (Figure 1) and increased Rac-driven actin polymerization in Y-27632 treated hIPSC-derived neurons.

The Y-27632-mediated significant decrease in neurite protrusion rates is more difficult to explain. If Rac-driven actin polymerization levels are increased and there are weaker NM-II-driven retraction forces present, we would expect faster neurite protrusion rates. Given results of the contrary, we believe this is due to another effect of ROCK inhibition. ROCK2 is also known to promote adhesion maturation in cell protrusions, resulting in focal adhesion formation [16, 39, 55]. Therefore, Y-27632-mediated ROCK inhibition may be decreasing the number of focal adhesions in neurite protrusions.

According to the “molecular clutch” hypothesis, actin filaments at the leading edge of a cell are “engaged” and immobilized when indirectly bound to transmembrane integrin proteins of the extracellular matrix (ECM) via focal adhesions [12]. Actomyosin-induced contractile forces are transmitted through these focal adhesions to the ECM, giving a cell traction [12]. As actin filaments polymerize at a cell’s leading edge, this allows a protrusion to form [12]. Contrastingly, in the absence of focal adhesions, actin filaments at the leading edge of a cell are “disengaged” with the ECM. As a result, traction forces are not generated and actomyosin-induced contractile forces instead cause actin retrograde flow, hindering cell protrusion events [12]. Thus, in the case of Y-27632 treated hIPSC-derived neurons, actin filaments may be “disengaged” from the ECM due to a lack of ROCK2-mediated focal adhesion formation. Consequently, neurite protrusion events halt until traction is regained via focal adhesion formation, leading to a decrease in neurite

protrusion rates (Figure 8B). Future experiments using ROCK isoform-specific knockdowns are needed to address this hypothesis.

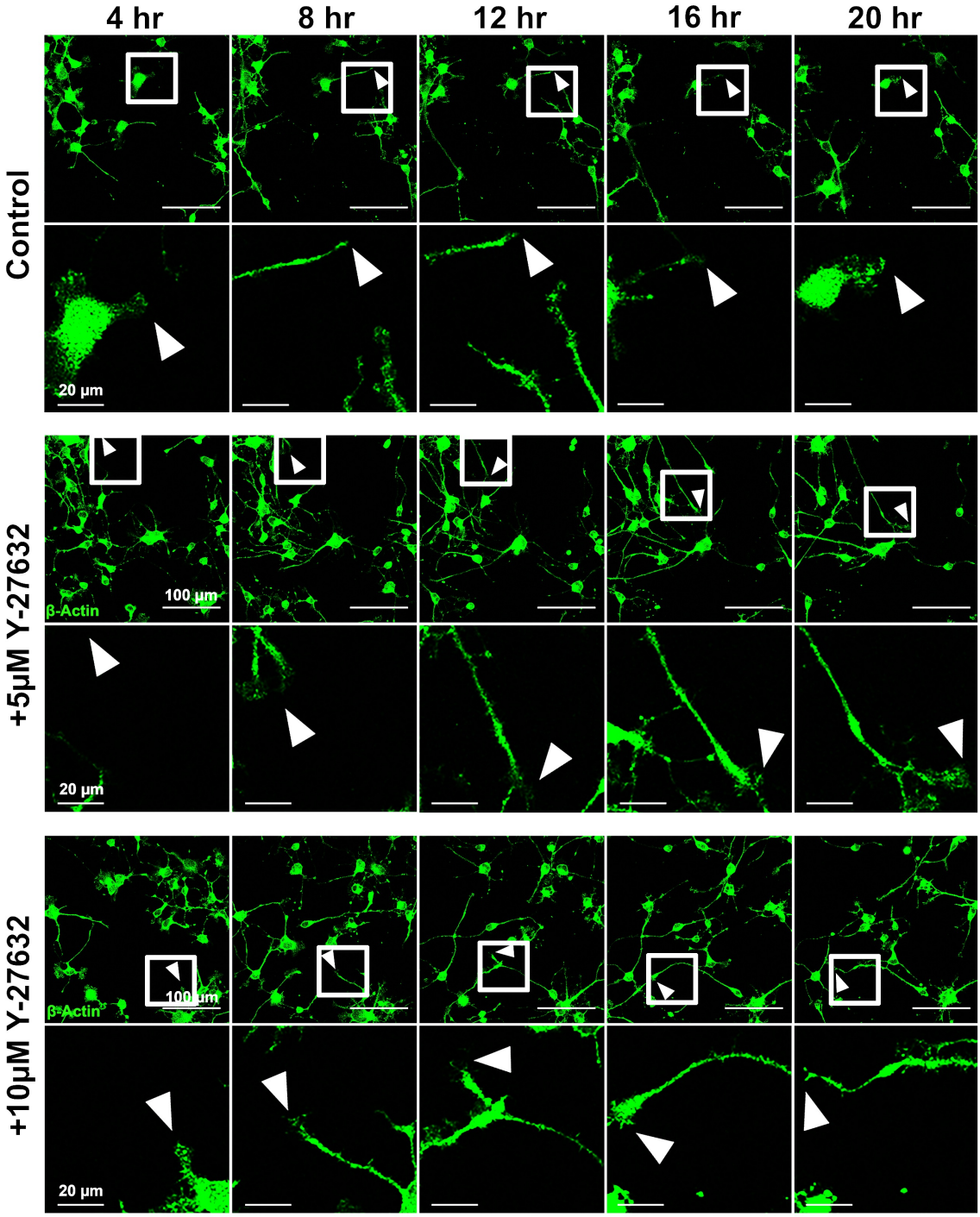

Figure 7. Neural Differentiation Time-Lapse. (A) Representative still frames of movies of neural differentiation of control cell line #3 hIPSC-derived NPCs gene-edited to express Actin mEGFP at 4, 8, 12, 16, and 20 hours following either 0µM (control), 5µM, or 10µM Y-27632 treatment. Insets included below each still frame. Y-27632 promotes neurite elongation (see white arrowheads). Experiment repeated three times.

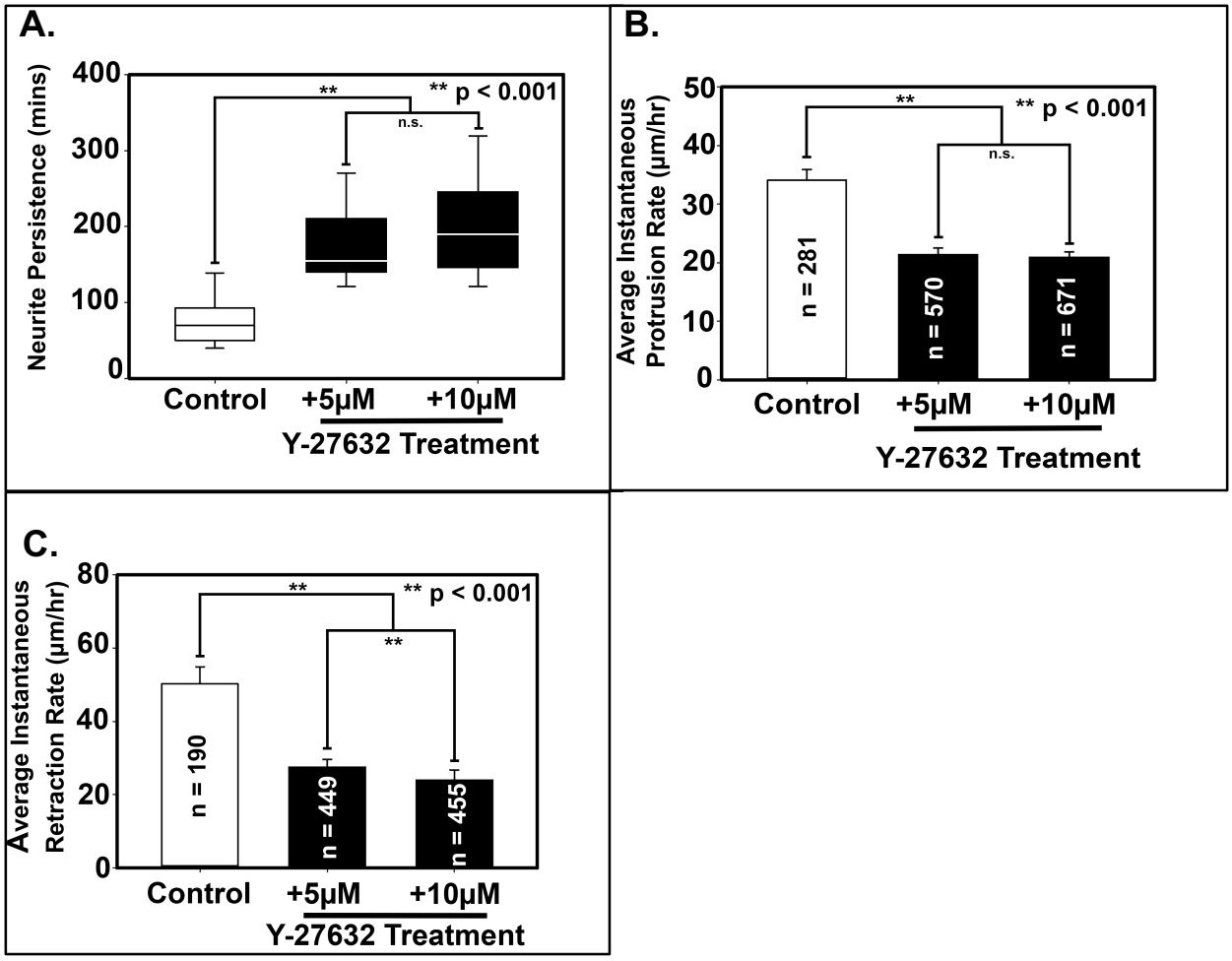

Figure 8. Y-27632 Significantly Increases Neurite Persistence and Significantly Decreases Neurite Protrusion and Retraction Rates. (A) Average persistence of neurites during 20 hour neural differentiation following treatment with either 0μM (control), 5μM, or 10μM of Y-27632 in control cell line #3 hIPSC-derived NPCs (n=30). (B) Average instantaneous protrusion rate of neurites during 20 hour neural differentiation following treatment with either 0μM (control), 5μM, or 10μM of Y-27632 in control cell line #3 hIPSC-derived NPCs (n values provided in graph). (C) Average instantaneous retraction rate of neurites during 20 hour neural differentiation following treatment with either 0μM (control), 5μM, or 10μM of Y-27632 in control cell line #3 hIPSC-derived NPCs (n values provided in graph). (n.s. not significant, ** $p < 0.001$) Experiment repeated three times.

Y-27632 Promotes Neurite Formation (3-D)

To determine if Y-27632-mediated ROCK inhibition promotes neurite formation in a more physiologically-relevant 'mini-brain' model as in 2-D hIPSC-derived neurons, three sets of approximately 90 day old control cell line #4 hIPSC-derived human cortical organoids were fixed, cryosectioned, and stained for the early neuronal marker doublecortin (DCX) to identify neurites and DAPI to identify nuclei.

Y-27632 treated 'mini-brains' visually appear to have more neurites as compared to control 'mini-brains' (Figure 9A). The average percent area of DCX normalized to DAPI significantly increased from 50.83% in control human cortical organoids to 124.80% in 10μM Y-27632 treated human cortical organoids (Figure 9B). Thus, Y-27632 may be promoting the formation of neurites in 3-D just as in 2-D hIPSC-derived neurons. This may be due to both an increase in number of neurites per neuron, neurite length, and branching.

The mechanism of this observation is likely due to the same proposed mechanism regarding the observed increase in number of neurites per neuron (Figure 4) and neurite length (Figure 5) in 2-D hIPSC-derived neurons. In 3-D, Y-27632-mediated ROCK1 and ROCK2 inhibition may decrease NM-II-driven contractility forces, resulting in an increase in neurite persistence as observed in 2-D hIPSC-derived neurons (Figure 7A). Increased neurite persistence leads to an increase in number of neurites per neuron. Furthermore, Y-27632-mediated ROCK2 inhibition may be upregulating Rac-driven actin polymerization, leading to the increased elongation of neurites.

A.

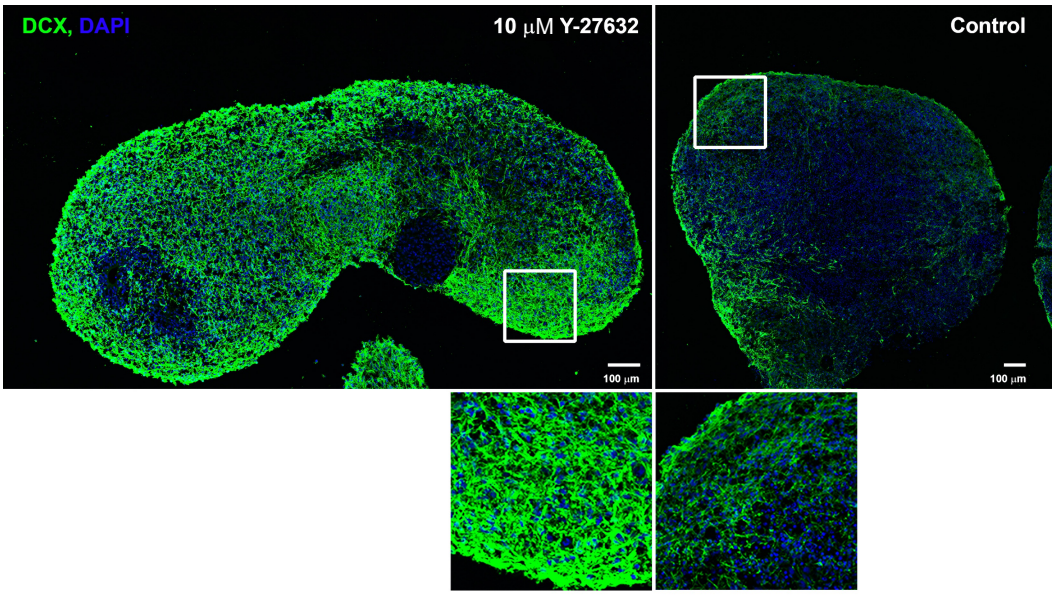

B.

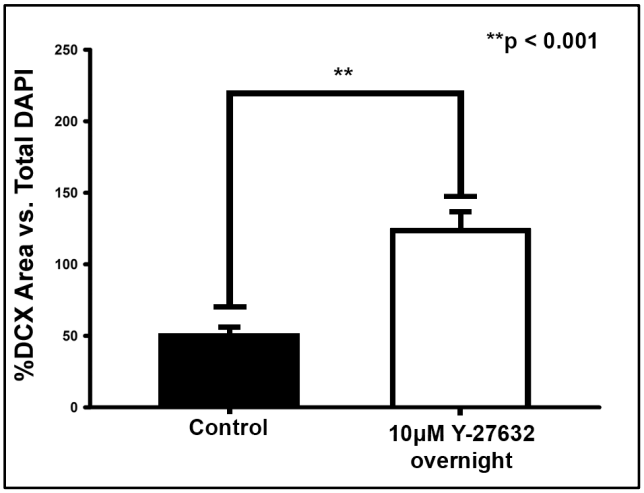

Figure 9. Y-27632 Significantly Increases Neurite Area. (A) 90 day old cerebral organoids treated with 10 μM Y-27632 overnight. 'Mini-brains' were cryosectioned and stained for the early neuronal marker, doublecortin (DCX, green), to label neurites, and the nuclei marker, DAPI (blue). (B) Y-27632 significantly increases the percent area of DCX normalized to DAPI (n=30, 2.5π mm^2 regions). Experiment repeated three times. ** $p < 0.001$

Y-27632 Remodels Excitatory Synapses (3-D)

To determine whether or not Y-27632 can be used to alter synaptic connections, three sets of approximately 90 day old control cell line #4 hIPSC-derived human cortical organoids were fixed, cryosectioned, and stained for the presynaptic excitatory synaptic marker vesicular glutamate transporter 1 (Vglut-1) and DAPI to identify nuclei.

Y-27632 treated ‘mini-brains’ visually appear to have more Vglut-1 expression as compared to control ‘mini-brains’ (Figure 10A). The average percent of Vglut-1 area normalized to DAPI significantly increased from 12.44% in control human cortical organoids to 46.00% in 10μM Y-27632 treated human cortical organoids (Figure 10B). Therefore, Y-27632 increases the density of excitatory synapses.

This result was very surprising at first. NM-II-driven contractility is necessary for bundling and contracting actin filaments, causing polarization and maturation of the dendritic spine head in 2-D rat hippocampal neurons [40]. Therefore, we initially hypothesize that less NM-II-driven contractility, via Y-27632-mediated ROCK1 and ROCK2 inhibition, would result in the formation of less mature mushroom shaped dendritic spines and excitatory synapses.

Given results to the contrary, RNA-Seq analysis of human cortical organoids was examined and we discovered that the ‘mini-brains’ preferentially expressed ROCK2 as opposed to ROCK1. Hence, we are inhibiting ROCK2 activity more than ROCK1 activity. Since ROCK2 is also known to inhibit Rac-driven actin polymerization [39], we may be increasing Rac-driven actin polymerization more than decreasing NM-driven contractility.

Although the dendritic spines of these Y-27632 treated ‘mini-brains’ may not be of the mature mushroom-shaped morphology, the spines heads may be larger due to increased Rac-driven actin polymerization [39, 52, 61]. This would give rise to an increase in excitatory synaptic area, as observed in the 10μM Y-27632 treated human cortical organoids. Further experiments exploring the Rac-driven actin polymerization pathway were completed to support this hypothesis.

A.

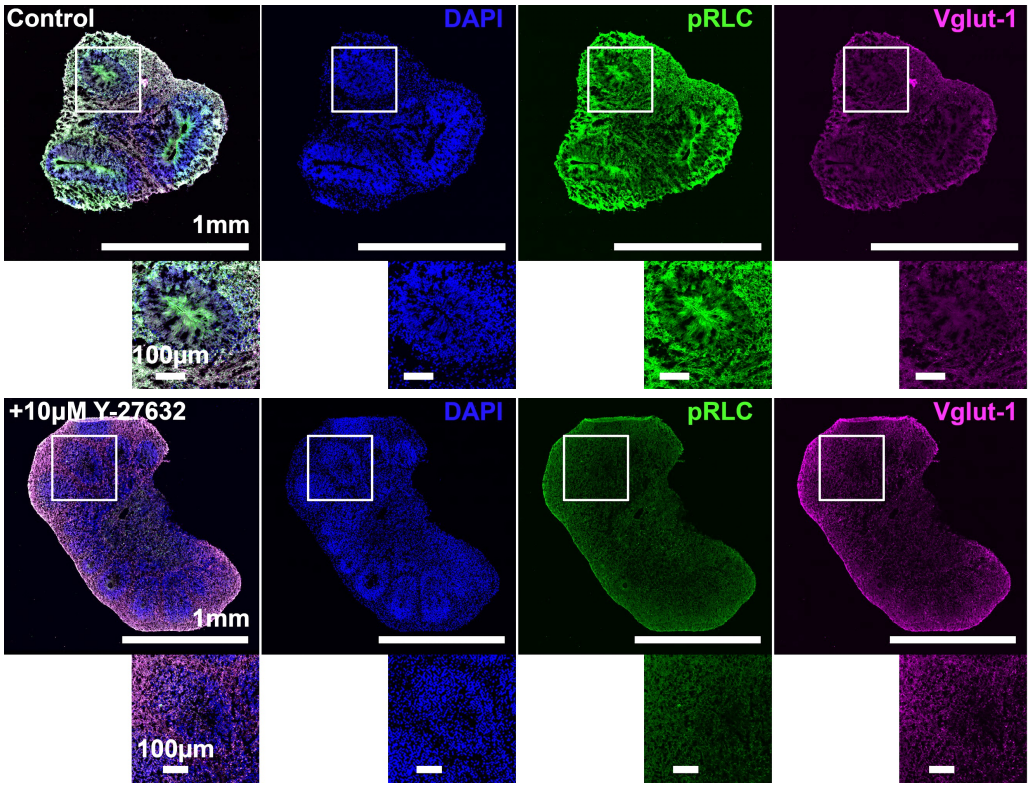

B.

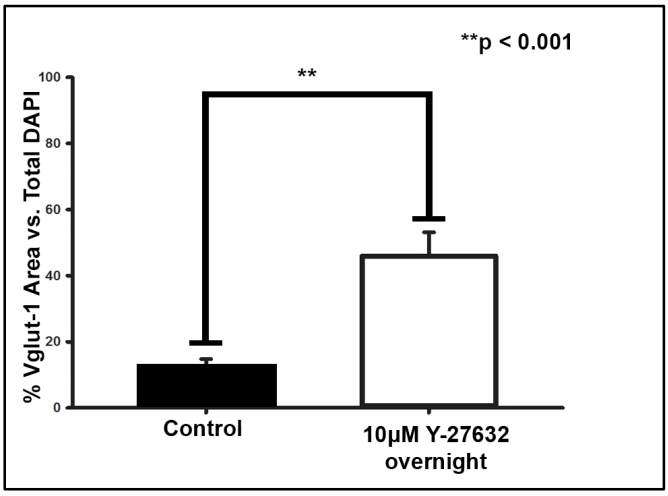

Figure 10. Y-27632 Significantly Increases Excitatory Synapse Area. (A) 90 day old 'mini-brains' were treated with 10µM Y-27632 for 24 hours. 'Mini-brains' were cryosectioned and stained with Vglut-1 (magenta) to identify excitatory synaptic contacts and pRLC (green) to identify phosphorylation of the ROCK substrate. (B) Y-27632 significantly increases the percent area of Vglut-1 normalized to DAPI (n=30, 2.5π mm^2 regions). Experiment repeated three times. ** $p < 0.001$

Y-27632 Increases Rac-driven Actin Polymerization (3-D)

To further support the hypothesis that increased Rac-driven actin polymerization drives the increase in excitatory synapse area, three sets of approximately 90 day old control cell line #4 hIPSC-derived human cortical organoids were fixed, cryosectioned, and stained for total LIM-Kinase 1 (LIMK), phosphorylated LIMK-Kinase 1 (pLIMK), and DAPI. Another three sets of approximately 90 day old hIPSC-derived human cortical organoids were fixed, cryosectioned, and stained for total cofilin, phosphorylated cofilin (pCofilin), and DAPI.

In the Rac-driven actin polymerization pathway, Rac1 activates p21-activated kinase (PAK) [25, 32] which phosphorylates and activates LIMK [Diagram 6] [10]. Subsequently, activated LIMK phosphorylates the actin severing protein cofilin to form pCofilin Ser3 [Diagram 6] [30]. This inhbits cofilin from associating with actin, leading to decreased actin turnover and increased actin polymerization [Diagram 6] [9]. Since we expect increased Rac-driven actin polymerization via Y-27632-mediated ROCK2 inhibition, we should see an increased ratio of percent area of pLIMK versus total LIMK in Y-27632 treated mini-brains [Diagram 6]. Furthermore, we should observe an increased ratio of percent area of pCofilin versus total cofilin [Diagram 6].

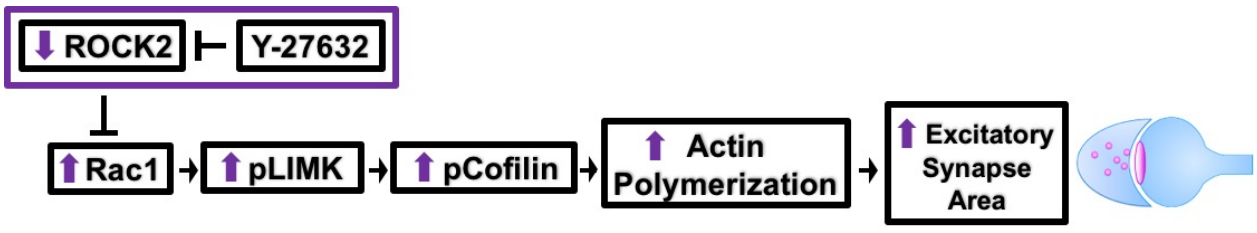

Diagram 6. Hypothesized Mechanism Underlying Synaptic Remodeling.

Y-27632 treated ‘mini-brains’ visually appear to have more pLIMK vs. total LIMK expression as compared to control ‘mini-brains’ (Figure 11A). The average percent area of pLIMK vs. total LIMK increased significantly from 23.77% in control human cortical organoids to 241.01% in 10μM Y-27632 treated human cortical organoids (Figure 11B). These results support the hypothesis of increased LIMK activity in the Rac-driven actin polymerization pathway. Note, the average percent area of pLIMK vs. total LIMK in 10μM Y-27632 treated human cortical organoids may be above 100% due to a stronger binding affinity of the pLIMK antibody compared to the LIMK antibody.

Y-27632 treated ‘mini-brains’ also visually appear to have more pCofilin vs. total cofilin expression as compared to control ‘mini-brains’ (Figure 12A). The average percent area of pCofilin vs. total cofilin increased significantly from 54.36% in control human cortical organoids to 93.07% in 10μM Y-27632 treated human cortical oganoids (Figure 12B). These results support the hypothesis of decreased cofilin activity in the Rac-driven actin polymerization pathway.

Together, these results provide evidence of a Y-27632-mediated increase in Rac-driven actin polymerization. Increased Rac-driven actin polymerization may cause expansion of the dendritic spine head, underlying the observed significant increase in the area of excitatory synapses in ‘mini-brains’ (Figure 10).

A.

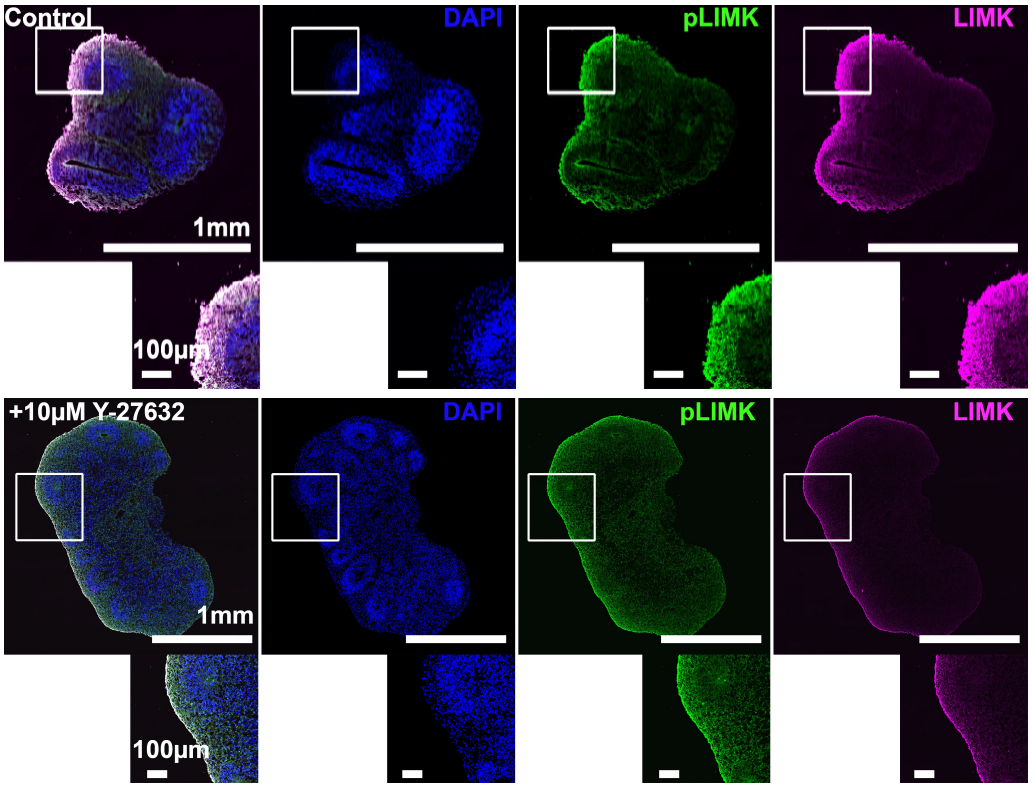

B.

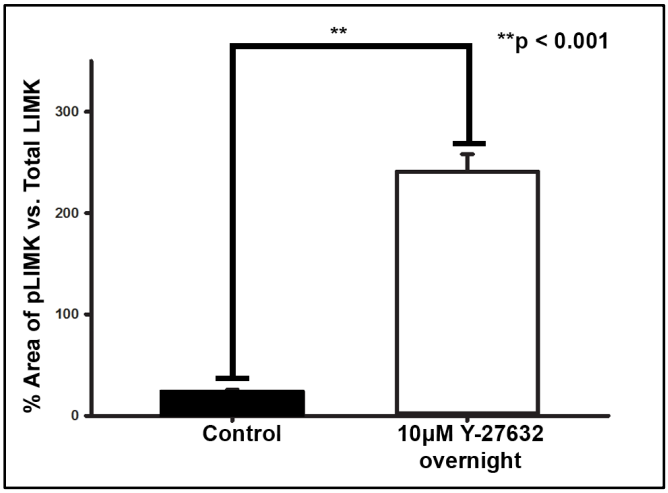

Figure 11. Y-27632 Significantly Increases LIMK Activation. Y-27632 stimulates Rac activation, leading to LIMK phosphorylation and activation. (A) 90 day old 'mini-brains' were treated with 10µM Y-27632 for 24 hours. 'Mini-brains' were cryosectioned and stained with pLIMK (green) and total LIMK (magenta). (B) Y-27632 significantly increases the percent area of pLIMK to total LIMK (n=30, 2.5π mm^2 regions). Experiment repeated three times.

A.

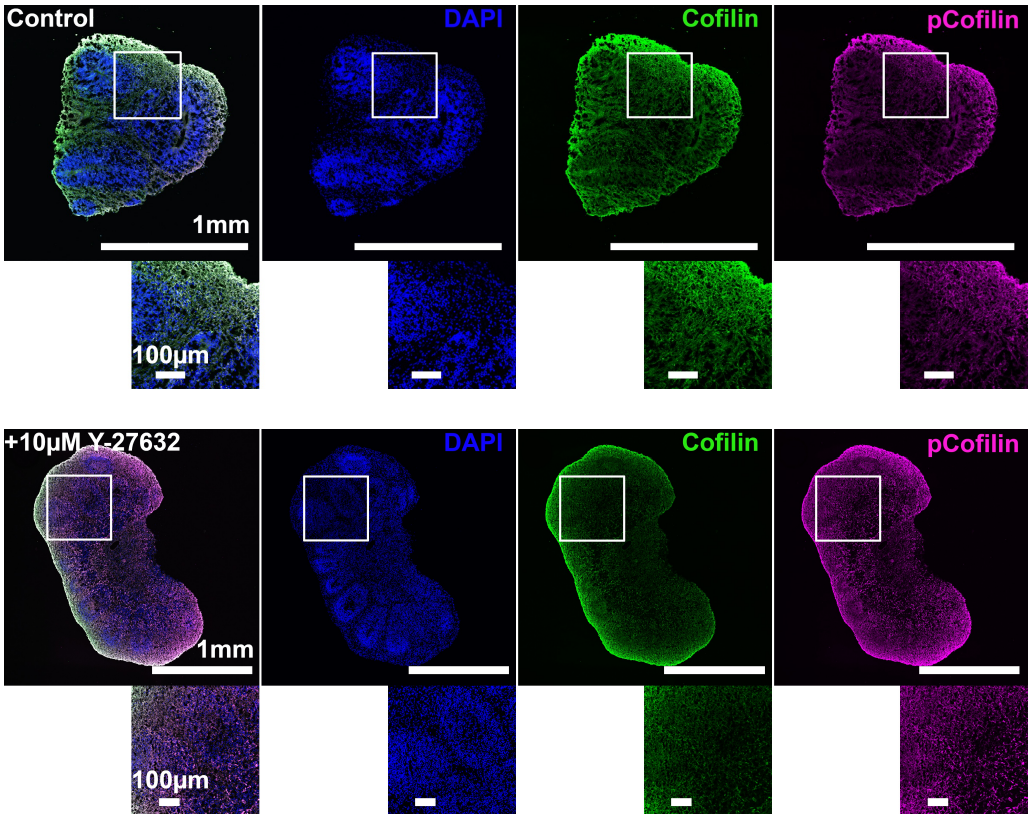

B.

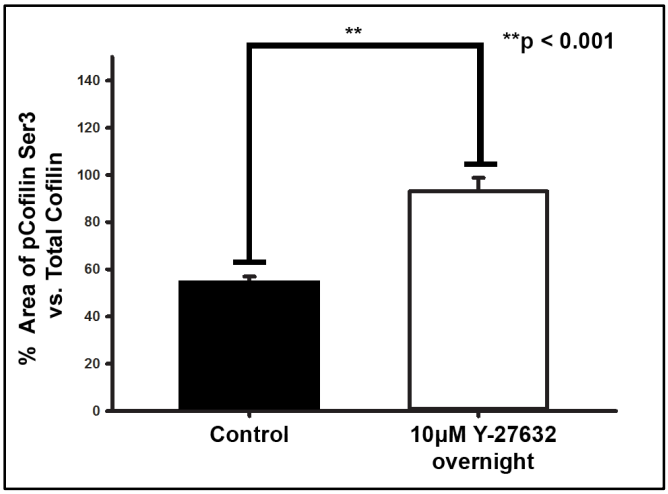

Figure 12. Y-27632 Significantly Decreases Cofilin Activation. Y-27632 promotes actin polymerization and stabilization via phosphorylation and inactivation of Cofilin by activated LIMK. (A) 90 day old 'mini-brains' were treated with 10µM Y-27632 for 24 hours. 'Mini-brains' were cryosectioned and stained for pCofilin Ser3 (magenta) and total Cofilin (green). (B) Y-27632 significantly increases the percent area of pCofilin Ser3 to total Cofilin (n=30, 2.5π mm^2 regions). Experiment repeated three times.

CHAPTER 4: DISCUSSION

Autism spectrum disorder (ASD) is a genetically complex heterogeneous neurodevelopmental disorder in which patients exhibit social deficits in both verbal and non-verbal forms of communication and display restricted and repetitive behaviors [2]. The etiology is unknown, but recent evidence suggests Autistic patients have increased densities of dendritic spines and increased numbers of excitatory to inhibitory synaptic connections, referred to as an E/I imbalance [42]. We sought to decrease this E/I imbalance in ASD patients by targeting the actin motor protein non-muscle myosin II (NM-II) due to its pivotal role of polarizing dendritic spines into a mature mushroom-shaped morphology, leading to synapse formation [Diagram 3] [16, 33, 39, 44]. Since the RhoA kinase serine/threonine effector Rho-Kinase (ROCK) phosphorylates and activates NM-II [1], we utilized a pan-ROCK inhibitor, Y-27632, to downregulate NM-II activity and potentially reduce the number of synaptic connections.

In this thesis work we utilized a more physiologically-relevant 3-D human cortical organoid (‘mini-brain’) model to explore the potential of Y-27632 as an ASD therapeutic and to improve our understanding of the mechanisms that underlie the formation of synaptic circuits. A recent study showed Y-27632 treatment of rat hippocampal neurons to increase the formation of filopodia-like spines [16]. Therefore, we hypothesized Y-27632-mediated ROCK inhibition would decrease synaptic connections in control ‘mini-brains.’ Surprisingly, acute Y-27632 treatment of ‘min-brains’ revealed an increase in excitatory synapse area (Figure 10).

To begin to explain this unexpected result, we analyzed control ‘mini-brain’ RNA-Seq data, which revealed a higher expression of the ROCK2 isoform as opposed to the ROCK1 isoform. Hence, we are inhibiting a higher level of ROCK2 as compared to ROCK1 with the isoform-nonselective ROCK inhibitor Y-27632. In addition to activating NM-II, ROCK2 inhibits Rac-driven actin polymerization [39], So we may be increasing Rac-driven actin polymerization levels within the ‘mini-brains’. Increased Rac-driven actin polymerization would cause expansion of the dendritic spine head, underlying the observed increase in excitatory synapse area (Figure 10).

To provide support for this hypothesis, we explored the Rac-driven actin polymerization pathway. We observed an increase in the area of phosphorylated LIMK-Kinase 1 (pLIMK) versus total LIMK-Kinase 1 (LIMK) (Figure 11) and phosphorylated cofilin (pCofilin) versus total cofilin (Figure 12) in the ‘mini-brains’. In the Rac-driven actin polymerization pathway, pLIMK phosphorylates the actin severing protein cofilin to form pCofilin [30]. This inhbits cofilin from associating with actin, leading to decreased actin turnover and increased actin polymerization [9]. Therefore, these results provide evidence of increased Rac-driven actin polymerization.

This hypothesis is further supported by a recent study in rat hippocampal neurons by Newell-Litwa et al. that revealed a ROCK2 knockdown-mediated increase in spine head size and excitatory synapse area as compared to ROCK1 knockdowns [39]. Interestingly, these ROCK1 knockdown neurons are morphologically similar to those observed by Hodges et al. in Y-27632 treated rat hippocampal neurons [16, 39]. Although unknown, rat hippocampal neurons may differentially express ROCK1 at higher levels

than ROCK2. If using rat hippocampal neurons as a model, this mistakenly provides further support for Y-27632 as a potential therapeutic in ASD patients. This demonstrates the need for physiologically-relevant brain models, such as ‘mini-brains’ to assess the impact of drug therapies on developing neural circuits.

In addition to altered synaptic connectivity, ASD patients express defective neurite formation [31]. Since ROCK inhibitors have been shown to increase neurite formation in many different 2-D cell cultures [13, 21, 29, 36, 46, 57], Y-27632 could potentially serve to rescue defective neurite formation in ASD patients. We first confirmed previous findings of a ROCK inhibitor-mediated increase in neurite formation using a human-induced (hIPSC)-derived neuron model. In this 2-D control cell model, we showed a Y-27632-mediated dose-dependent increase in the percent of neuronal cells (Figure 3), number of neurites per neuron (Figure 4), neurite length (Figure 5), and number of branch points per neurite (Figure 6).

In order to better understand the neurite dynamics and molecular mechanisms underlying these observed increases, we used a hIPSC-derived neuronal cell line previously gene-edited to express mEGFP to track neurite protrusion and retraction rates. The neurites of Y-27632 treated neurons protruded and retracted at a slower rate (Figures 7, 8B, 8C), leading to increased neurite persistence (Figures 7, 8A). We hypothesize slower retraction rates are due to decreased NM-II-driven contractile forces via ROCK1 and ROCK2 inhibition, while slower protrusion rates are due to decreased adhesion formation via ROCK2 inhibition.

We also examined the effects of Y-27632 on neurite formation in the more physiologically-relevant 3-D ‘mini-brain’ model. Acute Y-27632 treatment of control ‘mini-brains’ revealed an increase in area occupied by neurites (Figure 9). Therefore, Y-27632 increases neurite formation in 3-D just as in 2-D. These results support previous findings of the effects of ROCK inhibition on neurite formation and provide support for the potential of ROCK inhibitors as an ASD therapeutic during early neurite formation.

Although Y-27632-mediated ROCK inhibition increased neurite formation, it also increased excitatory synapses as mentioned previously. Together, these findings suggest Y-27632 would not serve as a potential therapeutic for ASD since we seek to decrease the number of excitatory connections in ASD patients. Instead, ROCK1 isoform-selective inhibitors may provide the answer. As observed by Newell-Litwa et al., rat hippocampal neurons exhibit a ROCK1 knockdown-mediated decrease in spine head size and excitatory synapse area as compared to ROCK2 knockdowns [39]. However, ROCK2 is more highly expressed in the developing human brain and brain organoids when compared to ROCK1 [Diagram 9] [22, 23, 43]. Thus, unlike rat hippocampal neurons, Y-27632 increases excitatory synapse area in brain organoids (Figure 10) consistent with knockdown of ROCK2. Therefore, a ROCK1 isoform-selective inhibitor may decrease the number of excitatory connections in ASD patients as opposed to pan-ROCK inhibitors such as Y-27632, that also inhibit ROCK2.

Despite the lack of evidence for Y-27632 as a potential ASD therapeutic, Y-27632 poses many other applications. Since Y-27632 increased the number of excitatory synapses in ‘mini-brains,’ we essentially recapitulated the E/I imbalance characteristic of

ASD patients. Thus, Y-27632 treated ‘mini-brains’ could be used as an alternative Autistic model for drug and gene therapies. Our current understanding of idiopathic Autism stems mainly from genomic analyses of blood and post-mortem patient brain samples [19, 26, 35, 37, 48, 58] and genetically modified mice models [37, 49]. However, the limited sample size of patient samples poses limitations. Furthermore, inherent genetic differences between mice and human brain circuits pose complications in applicability of conclusions drawn from ASD mice models [7, 37]. Alternatively, Y-27632 treated ‘mini-brains’ provide us with an applicable human-based and 3-D physiologically-relevant Autistic phenotypic cell model that requires limited sample sizes obtained by non-invasive methods.

Moreover, Y-27632 could potentially be used as a therapeutic in conditions where neural connections are lacking or lost, such as schizophrenia and Alzheimer’s disease. Y-27632 may increase neural connectivity in these diseases, particularly at the level of both neurites and synapses by the proposed mechanisms depicted in Diagrams 7 and 8 in Appendix D. Lastly, Y-27632 could potentially be used to lower elevated phosphorylated regulatory light chain (pRLC) levels in schizophrenic patients (Figure 1) [47].

REFERENCES

(1) Amano M, Ito M, Kimura K, Fukata Y, Chihara K, Nakano T, Matsuura Y, Kaibuchi K. (1996). Phosphorylation and activation of myosin by Rho-associated kinase (Rho-kinase). *J Biol Chem* 271(34): 20246-20249

(2) Autism Society (2016). What is Autism? Retrieved from http://www.autism-society.org/what-is/

(3) Baio J et al. (2014). Prevalence of Autism Spectrum Disorder Among Children Aged 8 Years. *MMWR Surveill Summ* 63(SS02): 1-21

(4) Baio J, Wiggins L, Christensen D.L, et al. (2018). Prevalence of Autism Spectrum Disorder Among Children Aged 8 Years. *MMWR Surveill Summ* 67(6): 1-23

(5) Brennand K.J, Simone A, Jou J, Gelboin-Burkhart C, Tran N, Sangar S, Li Y, Mu Y, Chen G, Yu D, McCarthy S, Sebat J, Gage F.H. (2011). *Nature* 473(7346): 221-225

(6) Chrzanowska-Wodnicka M, Burridge K. (1996). Rho-stimulated contractility drives the formation of stress fibers and focal adhesions. *J Cell Biol* 133(6): 1403-141

(7) DeFelipe J, Alonso-Nanclares L, Arellano J.I. (2002). Microstructure of the neocortex: comparative aspects. *J Neurocytol* 31(3-5): 299-316

(8) Dent E.W, Kwiatkowski A.V, Mebane L.M., Philippar U, Barzik M, Rubinson D.A, Gupton S, Van Veen J.E, Furman C, Zhang J et al. (2007). Filopodia are required for cortical neurite initiation. *Nat Cell Biol* 9(12): 1347-1359

(9) DesMarais V, Ghosh M, Eddy R, Condeelis J. (2005). Cofilin takes the lead. *J Cell Sci* 118(Pt 1):19-26

(10) Edwards D.C, Sanders L.C, Bokoch G.M, Gill G.N. (1999). Activation of LIM-kinase by Pak1 couples Rac/Cdc42 GTPase signalling to actin cytoskeletal dynamics. *Nat Cell Biol* 1(5): 253-259

(11) Fortin D.A, Davare M.A, Srivastava T, Brady J.D, Nygaard S, Derkach V.A, Soderling T.R. (2010). Long-term potentiation-dependent spine enlargement requires synaptic Ca2+-permeable AMPA receptors recruited by CaM-kinase I. *J Neurosci* 30(35): 11565-11575

(12) Gardel M.L, Schneider I.C, Aratyn-Schaus Y, Waterman C.M. (2015). Mechanical Integration of Actin and Adhesion Dynamics in Cell Migration. *Annu Rev Cell Dev Biol* 26: 315-333

(13) Gu H, Yu S.P, Gutekunst C.A, Gross R.E, Wei L. (2013). Inhibition of the Rho signaling pathway improves neurite outgrowth and neuronal differentiation of mouse neural stem cells. *Int J Physiol Pathophysiol Pharmacol* 5(1): 11-20

(14) Heasman S. J, Ridley A. J. (2008). Mammalian Rho GTPases: new insights into their functions from in vivo studies. *Nat Rev Mol Cell Biol* 9(9): 690-701

(15) Hedrick N.G, Harward S.C, Hall C.E, Murakoshi H, Mcnamara J.O, Yasuda R. (2016). Rho GTPase complementation underlies BDNF- dependent homo-and heterosynaptic plasticity The Rho GTPase proteins Rac1, RhoA and Cdc42 have a central role in regulating the actin cytoskeleton in dendritic spines. *Nature* 538(7623): 104-108

(16) Hodges J.L, Newell-Litwa K, Asmussen H, Vicente-Manzanares M, Horwitz A.R. (2011). Myosin IIB Activity and Phosphorylation Status Determines Dendritic Spine and Post-Synaptic Density Morphology. *PLoS One* 6(8): e24149

(17) Hotulainen P, Hoogenraad C.C. (2010). Actin in dendritic spines: connecting dynamics to function. *J Cell Biol* 189(4): 619-629

(18) Hotulainen P, Llano O, Smirnov S, Tanhuanpää K, Faix J, Rivera C, Lappalainen P. (2009). Defining mechanisms of actin polymerization and depolymerization during dendritic spine morphogenesis. *J Cell Biol* 185(2): 323-339

(19) Iossifov I, O'Roah B.J, Sanders S.J, et al. (2014). The contribution of de novo coding mutations to autism spectrum disorder. *Nature* 515(7526): 216-221

(20) Irie F, Yamaguchi Y. (2002). EphB receptors regulate dendritic spine development via intersectin, Cdc42 and N-WASP. *Nat Neurosci* 5(11): 1117-1118

(21) Jia X.F, Ye F, Wang Y.B, Feng D.X. (2016). ROCK inhibition enhances neurite outgrowth in neural stem cells by upregulating YAP expression in vitro. *Neural Regen Res* 11(6):983-987

(22) Johnson M.B, Imamura Kawasawa Y, Mason C.E, Krsnik Z, Coppola G, Bogdanovic D, Geschwind D.H, Mane S.M, State M.W, Sestan N. (2009). Functional and Evolutionary Insights into Human Brain Development through Global Transcriptome Analysis. *Neuron* 62(4): 494-509

(23) Kang H.J, Kawasawa Y.I, Cheng F, Zhu Y, Xu X, Li M. et al. (2011). Spatio-temporal transcriptome of the human brain. *Nature* 478(7370): 483-489

(24) Kimura K, Ito M, Amano M, Chihara K, Fukata Y, Nakafuku M, Yamamori B, Feng J, Nakano T, Okawa K, et al. (1996). Regulation of myosin phosphatase by Rho and Rho-associated kinase (Rho-kinase). *Science* 273(5272): 245-248

(25) Knaus U.G, Wang Y, Reilly A.M, Warnock D, Jackson J.H. (1998). Structural requirements for PAK activation by Rac GTPases. *J Biol Chem* 273(34): 21,512 - 21,518

(26) Konopka G, Friedrich T, Davis-Turak J, et al. (2012). Human-specific transcriptional networks in the brain. *Neuron* 75(4): 601-617

(27) Korobova F, Svitkina T. (2010). Molecular architecture of synaptic actin cytoskeleton in hippocampal neurons reveals a mechanism of dendritic spine morphogenesis. *Mol Biol Cell* 21(1): 165-176

(28) Kubo T, Hata K, Yamaguchi A, Yamashita T. (2007). Rho-ROCK inhibitors as emerging strategies to promote nerve regeneration. *Curr Pharm Des* 13(24): 2493-2499

(29) Lingor P, Teusch N, Schwarz K, Mueller R, Mack H, Bahr M, Mueller B.K. (2007). Inhibition of Rho kinase (ROCK) increases neurite outgrowth on chondroitin sulphate proteoglycan in vitro and axonal regeneration in the adult optic nerve in vivo. *J Neurochem* 103(1): 181-189

(30) Maekawa M, Ishizaki T, Boku S, Watanabe N, Fujita A, Iwamatsu A, Obinata T, Ohashi K, Mizuno K, Narumiya S. (1999). Signaling from Rho to the actin cytoskeleton through protein kinases ROCK and LIM-kinase. *Science* 285(5429): 895–898

(31) Maldergem L.V, Hou Q, Kalscheuer V.M, Rio M, Doco-Fenzy M, Medeira A, de Brouwer A.P.M, Cabrol C, Haas S.A, Cacciagli P, Moutton S, Landais E, Motte J, Colleaux L, Bonnet C, Villard L, Dupont J, Man H.Y. (2013). Loss of function of *KIAA2022* causes mild to severe intellectual disability with an autism spectrum disorder and impairs neurite outgrowth. *Human Molecular Genetics* 22(16): 3306-3314

(32) Manser E, Leung T, Salihuddin H, Zhao Z.S, Lim L. (1994). A brain serine/threonine protein kinase activated by Cdc42 and Rac1. *Nature* 367(6458): 40-46

(33) Martin-Vilchez S, Whitmore L, Asmussen H, Zareno J, Horwitz R, Newell-Litwa K. (2017). RhoGTPase Regulators Orchestrate Distinct Stages of Synaptic Development. *PLoS One* 12(1): e0170464

(34) Menna E, Disanza A, Cagnoli C, Schenk U, Gelsomino G, Frittoli E, Hertzog M, Offenhauser N, Sawallisch C, Kreienkamp H.J et al. (2009). Eps8 regulates axonal filopodia in hippocampal neurons in response to brain-derived neurotrophic factor (BDNF). *PLoS Biol* 7(6): e100013

(35) Miller J.A, Ding S.L, Sunkin S.M, et al. (2014). Transcriptional Landscape of the Prenatal Human Brain. *Nature* 508(7495): 199-206

(36) Minase T, Ishima T, Itoh K, Hashimoto K. (2010). Potentiation of nerve growth factor-induced neurite outgrowth by the ROCK inhibitor Y-27632: a possible role of IP_3 receptors. *Eur J Pharmacol* 648(1-3): 67-73

(37) Muotri A.R. (2016). The human model: changing focus on autism research. *Biol Psychiatry* 79(8): 642-649

(38) Nadif Kasri N, Van Aelst L. (2008). Rho-linked genes and neurological disorders. *Pflugers Arch* 455(5): 787-797

(39) Newell-Litwa K.A, Badoual M, Asmussen H, Patel H, Whitmore L, Horwitz A.R. (2015). ROCK1 and 2 differentially regulate actomyosin organization to drive cell and synaptic polarity. *J Cell Biol* 210(2): 225-242

(40) Newell-Litwa K.A, Horwitz R, Lamers M.L. (2015). Non-muscle myosin II in disease: mechanisms and therapeutic opportunities. *Dis Model Mech* 8(12): 1495-1515

(41) Paşca A.M, Sloan S.A, Clarke L.E, Tian Y, Makinson C.D, Huber N, Kim C.H, Park J.Y, O'Rourke N.A, Nguyen K.D, Smith S.J, Huguenard J.R, Geschwind D.H, Barres B.A, Pasca S.P. (2015). Functional cortical neurons and astrocytes from human pluripotent stem cells in 3D culture. *Nat Methods* 12: 671–678.

(42) Penzes P, Cahill M.E, Jones K.A, VanLeeuwen J.E, Woolfrey K.M. (2011). Dendritic spine pathology in neuropsychiatric disorders. *Nat Neurosci* 14(3): 285–293

(43) Pletikos M, Sousa A.M, Sedmak G, Meyer K.A, Zhu Y, Cheng F, Li M, Kawasawa Y.I, Sestan N. (2014). Temporal specification and bilaterality of human neocortical topographic gene expression. *Neuron* 81(2): 321-332

(44) Rex C.S, Chen L.Y, Sharma A, Liu J, Babayan A.H, Gall C.M, Lynch G. (2009). Different Rho GTPase-dependent signaling pathways initiate sequential steps in the consolidation of long-term potentiation. *J Cell Biol* 186(1): 85-97

(45) Rice C et al. (2007). Prevalence of Autism Spectrum Disorders. *MMWR Surveill Summ* 56(SS01): 1-11

(46) Roloff F, Scheiblich H, Dewitz C, Dempewolf S, Stern M, Bicker G. (2015). Enhanced neurite outgrowth of human model (NT2) neurons by small-molecule inhibitors of Rho/ROCK signaling. *PLoS One* 10(2): e0118536

(47) Rubio M.D, Haroutunian V, Meador-Woodruff J.H. (2012). Abnormalities of the Duo/Rac-1/PAK1 Pathway Drive Myosin Light Chain Phosphorylation in Frontal Cortex in Schizophrenia. *Biol Psychiatry* 71(10): 906-914

(48) Sebat J, Lakshmi B, Malhotra D, et al. (2007). Strong Association of De Novo Copy Number Mutations with Autism. *Science* 316(5823): 445-449

(49) Silverman J.L, Yang M, Lord C, Crawly J.N. (2010). Behavioural phenotyping assays for mouse models of autism. *Nat Rev Neurosci* 11(7): 490-502

(50) Takahashi K, Tanabe K, Ohnuki M, Narita M, Ichisaka T, Tomoda K, Yamanaka S. (2007). Induction of pluripotent stem cells from adult human fibroblasts by defined factors. *Cell* 131(5): 861-872

(51) Tan H.B, Zhong Y.S, Cheng Y, Shen X. (2011.) Rho/ROCK pathway and neural regeneration: a potential therapeutic target for central nervous system and optic nerve damage. *Int J Ophthalmol* 4(6): 652-657

(52) Tashiro A, Yuste R. (2004). Regulation of dendritic spine motility and stability by Rac1 and Rho kinase: evidence for two forms of spine motility. *Mol Cell Neurosci* 26(3): 429-440

(53) Todorovski Z, Asrar S, Liu J, Saw NMN, Joshi K, Cortez M.A, Snead OC, Xie W, Jia Z. (2015). LIMK1 Regulates Long-Term Memory and Synaptic Plasticity via the Transcriptional Factor CREB. *Mol Cell Biol* 35(8): 1316-1328

(54) Vicente-Manzanares M, Hodges J, Horwitz A.R. (2009). Dendritic Spines: Similarities with Protrusions and Adhesions in Migrating Cells. *Open Neurosci J* 3: 87–96

(55) Vicente-Manzanares M, Horwitz A.R. (2010). Myosin light chain mono- and di-phosphorylation differentially regulate adhesion and polarity in migrating cells. *Biochem Biophys Res Commun* 402(3): 537-542

(56) Wilkinson S, Paterson H. F, Marshall C. J. (2005). Cdc42-MRCK and Rho-ROCK signalling cooperate in myosin phosphorylation and cell invasion. *Nat Cell Biol* 7(3): 255-261

(57) Yang P, Wen H.Z, Zhang J.H. (2010). Expression of a dominant-negative Rho-kinase promotes neurite outgrowth in a microenvironment mimicking injured central nervous system. *Acta Pharmacol Sin* 31(5): 531-539

(58) Yuen R.K, Thiruvahindrapuram B, Merico D, et al. (2015). Whole-genome sequencing of quartet families with autism spectrum disorder. *Nat Med* 21(2): 185-191

(59) Yuste R, Bonhoeffer T. (2004). Genesis of dendritic spines: insights from ultrastructural and imaging studies. *Nat Rev Neurosci* 5(1): 24-34

(60) Yuste R. (2013). Electrical Compartmentalization in Dendritic Spines. *Annu Rev Neurosci* 36: 429-449

(61) Zhang H, Macara I.G. (2006). The polarity protein PAR-3 and TIAM1 cooperate in dendritic spine morphogenesis. *Nat Cell Biol* 8(3): 227-237

APPENDIX A: PRIMARY AND SECONDARY ANTIBODIES

Primary Antibody	Brand	Catalog Number	Host	Class	Dilution	Concentration Used
Ankyrin G	UC Davis/ NIH NeuroMab Facility	75-146	Mouse IgG	Monoclonal	1:500*	N/A
ß-III Tubulin	R&D Systems®	MAB1195	Mouse IgG	Monoclonal	1:500*	1µg/mL
Cofilin	Cell Signaling Technology®	5175S	Rabbit IgG	Monoclonal	1:500*	N/A
Doublecortin	abcam	ab153668	Chicken IgY	Polyclonal	1:100*	2µg/mL
LIMK1	abcam	ab119084	Mouse IgG2b	Monoclonal	1:100*	N/A
Myosin Light Chain	Sigma Aldrich®	M4401	Mouse IgM	Monoclonal	1:250*	N/A
Myosin phospho- (S19/S20)	Rockland™	600-401-416	Rabbit IgG	Polyclonal	1:500*	2µg/mL
Phospho-Cofilin (Ser3)	Cell Signaling Technology®	3313S	Rabbit IgG	Monoclonal	1:500*	N/A
Phospho-LIMK1 (Thr508)	Invitrogen™	PA5-37629	Rabbit IgG	Polyclonal	1:100*	10µg/mL
Vglut-1	Synaptic Systems	135 304	Guinea Pig IgG	Polyclonal	1:1,000*	N/A

Table 1. Primary Antibodies
* IHC

Secondary Antibody	Brand	Catalog Number	Host	Class	Dilution	Concentration Used
Anti-Chicken Alexa Fluor® 488	Invitrogen™	A-11039	Goat IgG	Polyclonal	1:500*	4µg/mL
Anti-Guinea Pig Alexa Fluor® 568	Invitrogen™	A-11075	Goat IgG	Polyclonal	1:500*	4µg/mL
Anti-Guinea Pig Alexa Fluor® 647	Invitrogen™	A-21450	Goat IgG	Polyclonal	1:500*	4µg/mL
Anti-Mouse Alexa Fluor® 488	Invitrogen™	A-11001	Goat IgG	Polyclonal	1:500*	4µg/mL
Anti-Mouse Alexa Fluor® 568	Invitrogen™	A-11004	Goat IgG	Polyclonal	1:500*	4µg/mL
Anti-Mouse Alexa Fluor® 647	Invitrogen™	A-21235	Goat IgG	Polyclonal	1:500*	4µg/mL
Anti-Mouse Alexa Fluor® 488 IgM	Invitrogen™	A-21042	Goat IgG	Polyclonal	1:500*	4µg/mL
Anti-Rabbit Alexa Fluor® 488	Invitrogen™	A-11008	Goat IgG	Polyclonal	1:500*	4µg/mL
Anti-Rabbit Alexa Fluor® 568	Invitrogen™	A-11011	Goat IgG	Polyclonal	1:500*	4µg/mL
Anti-Rabbit Alexa Fluor® 647	Invitrogen™	A-21245	Goat IgG	Polyclonal	1:500*	4µg/mL

Table 2. Secondary Antibodies
* IHC

APPENDIX B: ABSOLUTE AVERAGES

Group	Figure 3A	Figure 3B	Figure 3C
Control	43.96	51.47	62.94
5μM	59.43	67.18	72.91
10μM	68.30	73.60	74.62
25μM	64.09	72.76	75.09
50μM	64.04	74.28	74.74

Table 3. Figure 3 Average Percent of Neuronal Cells

Group	Figure 4A	Figure 4B	Figure 4C
Control	1.47	1.45	1.53
5μM	1.46	1.49	1.68
10μM	1.53	1.56	1.70
25μM	1.48	1.56	1.68
50μM	1.50	1.58	1.73

Table 4. Figure 4 Average Number of Neurites per Neuron

Group	Figure 5A	Figure 5B	Figure 5C
Control	29.97	38.64	29.18
5μM	33.30	46.26	35.28
10μM	37.62	50.19	37.58
25μM	36.60	49.74	38.87
50μM	38.00	51.50	40.80

Table 5. Figure 5 Average Neurite Length (μm)

Group	Figure 6A	Figure 6B	Figure 6C
Control	0.34	0.53	0.31
5μM	0.38	0.69	0.47
10μM	0.44	0.75	0.53
25μM	0.39	0.77	0.54
50μM	0.43	0.79	0.58

Table 6. Figure 6 Average Number of Branch Points

APPENDIX C: MULTIPLE COMPARISONS STATISTICS

Comparison	Figure 1A	Figure 1B
50μM vs. Control	<0.001**	<0.001**
50μM vs. 5μM	<0.001**	<0.001**
50μM vs. 10μM	<0.001**	<0.001**
50μM vs. 25μM	<0.001**	<0.001**
25μM vs. Control	<0.001**	<0.001**
25μM vs. 5μM	<0.001**	<0.001**
25μM vs. 10μM	<0.001**	<0.001**
10μM vs. Control	<0.001**	<0.001**
10μM vs. 5μM	<0.001**	<0.001**
5μM vs. Control	<0.001**	<0.001**

Table 7. Figure 1 p Values. ** $p < 0.001$ * $p < 0.05$

Comparison	Figure 3A	Figure 3B	Figure 3C
50μM vs. Control	<0.001**	<0.001**	<0.001**
50μM vs. 5μM	<0.001**	<0.001**	<0.001**
50μM vs. 10μM	<0.001**	0.483	1.000
50μM vs. 25μM	1.000	<0.001**	1.000
25μM vs. Control	<0.001**	<0.001**	<0.001**
25μM vs. 5μM	<0.001**	<0.001**	<0.001**
25μM vs. 10μM	<0.001**	0.121	1.000
10μM vs. Control	<0.001**	<0.001**	<0.001**
10μM vs. 5μM	<0.001**	<0.001**	<0.001**
5μM vs. Control	<0.001**	<0.001**	<0.001**

Table 8. Figure 3 p Values. ** $p < 0.001$ * $p < 0.05$

Comparison	Figure 4A	Figure 4B	Figure 4C
50μM vs. Control	<0.001**	<0.001**	<0.001**
50μM vs. 5μM	<0.001**	<0.001**	<0.001**
50μM vs. 10μM	<0.001**	0.040*	<0.001**
50μM vs. 25μM	<0.001**	0.002*	<0.001**
25μM vs. Control	0.163	<0.001**	<0.001**
25μM vs. 5μM	0.223	<0.001**	1.000
25μM vs. 10μM	<0.001**	1.000	0.002*
10μM vs. Control	<0.001**	<0.001**	<0.001**
10μM vs. 5μM	<0.001**	<0.001**	<0.001**
5μM vs. Control	1.000	<0.001**	<0.001**

Table 9. Figure 4 p Values. ** $p < 0.001$ * $p < 0.05$

Comparison	Figure 5A	Figure 5B	Figure 5C
50μM vs. Control	<0.001**	<0.001**	<0.001**
50μM vs. 5μM	<0.001**	<0.001**	<0.001**
50μM vs. 10μM	1.000	0.177	<0.001**
50μM vs. 25μM	1.000	<0.001**	<0.001**
25μM vs. Control	<0.001**	<0.001**	<0.001**
25μM vs. 5μM	<0.001**	<0.001**	<0.001**
25μM vs. 10μM	0.056	0.196	<0.001**
10μM vs. Control	<0.001**	<0.001**	<0.001**
10μM vs. 5μM	<0.001**	<0.001**	<0.001**
5μM vs. Control	<0.001**	<0.001**	<0.001**

Table 10. Figure 5 p Values. ** $p < 0.001$ * $p < 0.05$

Comparison	Figure 6A	Figure 6B	Figure 6C
50μM vs. Control	<0.001**	<0.001**	<0.001**
50μM vs. 5μM	<0.001**	<0.001**	<0.001**
50μM vs. 10μM	0.154	<0.001**	<0.001**
50μM vs. 25μM	<0.001**	0.026*	<0.001**
25μM vs. Control	<0.001**	<0.001**	<0.001**
25μM vs. 5μM	0.010*	<0.001**	<0.001**
25μM vs. 10μM	<0.001**	1.00	1.00
10μM vs. Control	<0.001**	<0.001**	<0.001**
10μM vs. 5μM	<0.001**	<0.001**	<0.001**
5μM vs. Control	<0.001**	<0.001**	<0.001**

Table 11. Figure 6 p Values. ** $p < 0.001$ * $p < 0.05$

APPENDIX D: PROPOSED MECHANISMS

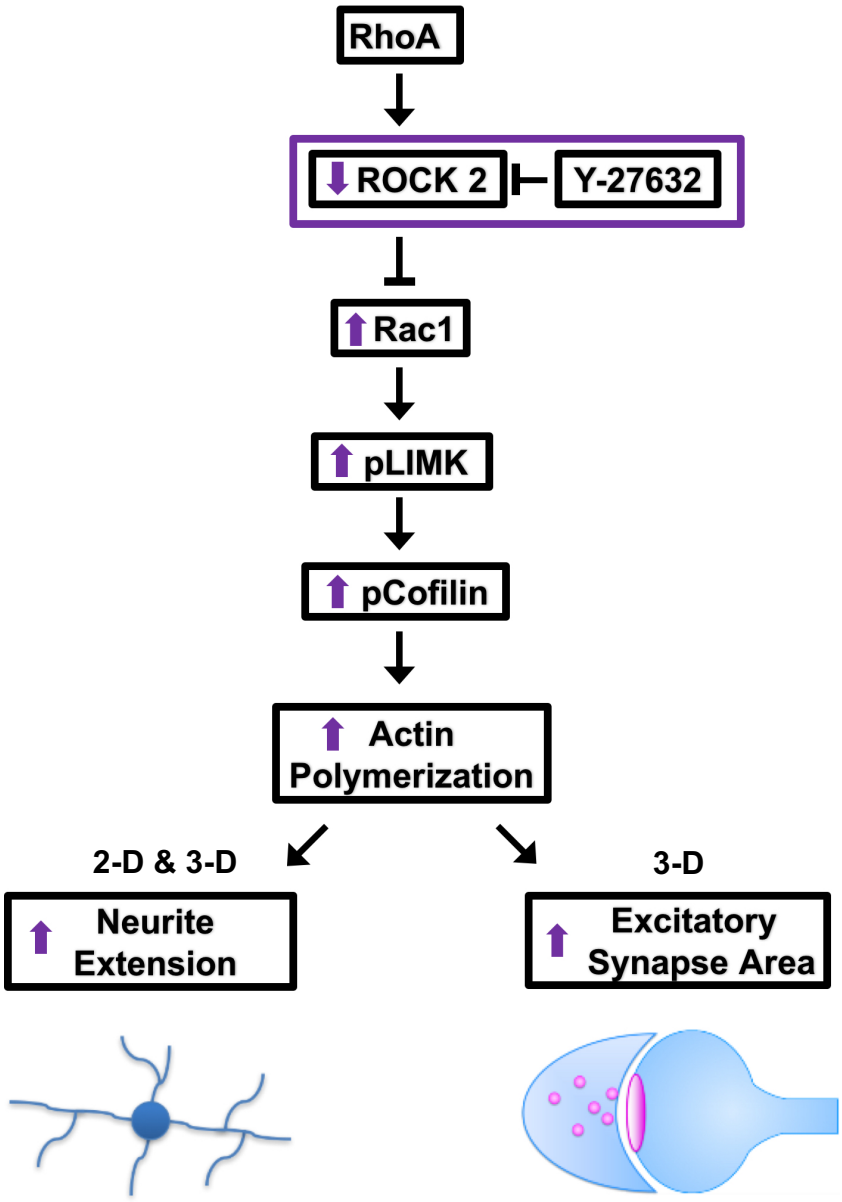

Diagram 7. Y-27632 Increases Rac-driven Actin Polymerization. ROCK2 inhibits Rac-driven actin polymerization. Thus, Y-27632-mediated ROCK2 inhibition causes upregulation of the Rac-driven actin polymerization pathway. In particular, increased LIMK-1 activity leads to phosphorylation and inactivation of the actin severing protein cofilin, promoting actin stabilization and polymerization. In 2-D hIPSC-derived neurons and 3-D 'mini-brains', this promotes neurite formation. In 3-D 'mini-brains', this mechanism increases excitatory synapse area by increasing the size of the dendritic spine head.

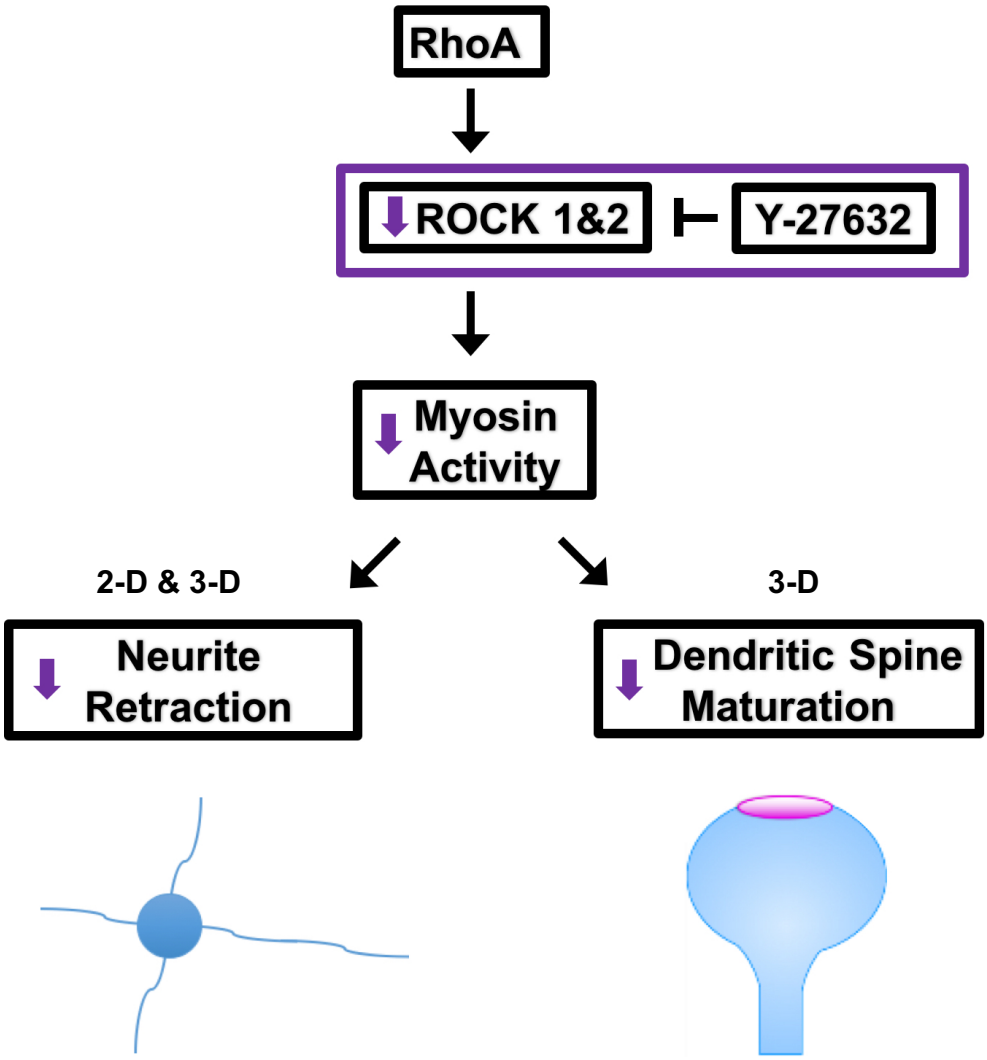

Diagram 8. Y-27632 Decreases NM-II-driven Contractility. Y-27632-mediated ROCK1 and ROCK2 inhibition downregulates NM-II activity, leading to less actomyosin-driven contractility forces. In 2-D hIPSC-derived neurons and 3-D 'mini-brains', this promotes neurite formation. In 3-D 'mini-brains', this mechanism results in less mature mushroom-shaped dendritic spines.

APPENDIX E: TRANSCRIPTOMICS

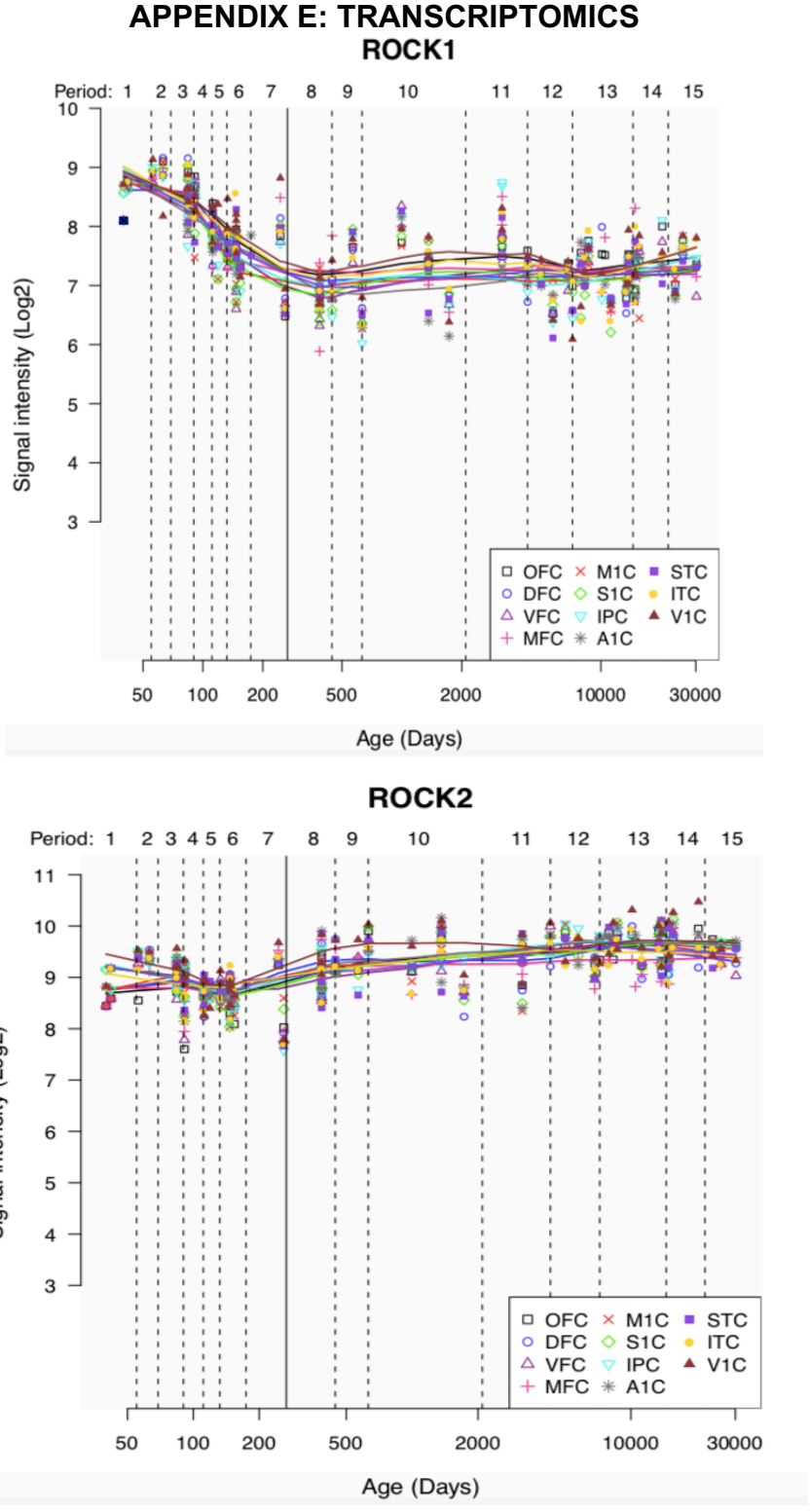

Diagram 9. ROCK1 vs. ROCK2 Expression in the Human Neocortex. [Retrieved from hbatlas.org] [22, 23, 43]